Atomic Conformational Dynamics and Actin-Crosslinking Function of Alpha-Actinin Revealed by SimHS-AFMfit

Kien Xuan Ngo[1,5,6,*], Takashi Sumikama[1, 6,*], Rémi Vuillemot[2,*], Han Gia Nguyen[1], Taro QP Uyeda[3], Ngan Thi Phuong Le[4], Sergei Grudinin[2,*]

[1]Nano Life Science Institute (WPI-NanoLSI), Kanazawa University, Kanazawa, Japan.

[2]Univ. Grenoble Alpes, CNRS, Grenoble INP, LJK, 38000 Grenoble, France.

[3]Faculty of Advanced Science and Engineering, Waseda University, Shinjuku, Japan.

[4]Center for Bioscience and Biotechnology, University of Science, Vietnam National University, Ho Chi Minh City, Vietnam

[5]Lead contact

[6]These authors contributed equally.

*Corresponding author: Kien Xuan Ngo, Takashi Sumikama, Rémi Vuillemot, Sergei Grudinin

Email:

ngoxuankien@staff.kanazawa-u.ac.jp (K.X.N.)

sumi@staff.kanazawa-u.ac.jp (T.S.)

remi.vuillemot@univ-grenoble-alpes.fr (R.V.)

sergei.grudinin@univ-grenoble-alpes.fr (S.G.)

Abstract

Alpha-actinin is a crucial actin-binding protein involved in cellular functions like muscle contractility, mechanosensation, and cell division. Studying its atomic structure and dynamics is challenging due to protein complexity and imaging limitations. To address this, we developed **SimHS-AFMfit**, integrating high-speed AFM (HS-AFM), AFMfit (a flexible fitting technique), and molecular dynamics (MD) simulations. This approach successfully converted 2D AFM images into 3D atomic conformations, revealing the atomic conformational dynamics of Ca^{2+}-bound and unbound alpha-actinin. Using principal component analysis, we classified and quantified protein motions such as twisting and bending. HS-AFM and MD simulations further characterized the fluctuations of rise and axial distance (AD) between adjacent protomers in actin filament crosslinking models, identifying structural features that regulate myosin II and cofilin binding. These findings enhance our understanding of alpha-actinin's role in actin filament modulation and provide insights for studying more complex protein assemblies, such as contractile rings.

Keywords:

Alpha-actinin, Actin, Cofilin, Myosin II, unipolar-bipolar crosslinking, HS-AFM, AFMfit, MD Simulations, SimHS-AFMfit, PCA.

Alpha-actinin is a key protein in the organization of the actin cytoskeleton and is crucial for maintaining the mechanical properties of cells. In humans, alpha-actinin isoforms 2 and 3, which are believed to be Ca^{2+} insensitive, are integral to the function of striated muscle and are regulated by phosphoinositides[1–6]. In contrast, non-muscle alpha-actinin isoforms 1 and 4 are Ca^{2+}-sensitive[7–9]. Previous studies have elucidated the atomic structure of these muscle and non-muscle alpha-actinin isoforms via techniques such as X-ray scattering[7–9]; however, these methods often fail to capture the dynamic conformational changes of these molecules. An understanding of these changes is crucial for elucidating the role of alpha-actinin in actin filament crosslinking and the associated structural changes under unipolar and bipolar crosslinking states.

Actin is one of the most highly conserved eukaryotic proteins; when formed into filaments, actin plays a crucial role in various cellular processes, including morphogenesis, motility, division, intracellular transport, and membrane deformation in the cytosol[10]. These filaments also contribute to the nuclear functions such as transcriptional regulation, chromatin remodeling, and DNA repair[11]. Consequently, a key goal in biology and biophysics is to elucidate the molecular mechanisms governing the functional differentiation of the actin filaments within the cells. Actin filaments are right-handed helices, and their subunits are arranged in a way that generates two distinct pitches: a major pitch and a minor pitch. The major pitch represents the overall helical turn or a half helix of the filament and spans approximately 36 nm or approximately 13 subunits (6.5 protomer pairs) in the canonical actin filament[12–17]. The minor pitch, on the other hand, refers to the smaller, localized helical twist between adjacent G-actin subunits within one turn of the major helix and is approximately 5.5 nm[13–16]. These two structural features are fundamental to the establishment of the mechanical properties of the actin filaments[18,19], influencing their flexibility and stability[20,21]. Moreover, they play essential roles in regulating the binding interactions of proteins such as cofilin and myosin II, V, debrin, fimbrin, and Rng2-CHD[17,22,31,23–30].

The primary challenge in studying protein dynamics at atomic resolutions in real time using atomic force microscopy (AFM) lies in bridging gaps at the temporal and spatial scales. While high-speed AFM (HS-AFM) can capture the dynamics of the two-dimensional (2D) surface structures of proteins with optimal performance in just a few tens of milliseconds (~20 ms/frame) and at nanometer scales (1 nm in the x–y plane; ~0.1 nm in the z–direction)[22,24,32–38], conventional molecular dynamics (MD) simulations typically explore atomic structures over much shorter time scales, from femtoseconds to microseconds[39–41]. Protein dynamics span a wide range of temporal scales (fs-μs), reflecting movements from atomic vibrations to molecular tumbling and larger collective motions that can be observed with nuclear magnetic resonance (NMR)[42,43] and MD simulations[40,44–48]. However, HS-AFM is particularly valuable for investigating slower processes, such as protein folding and conformational changes induced by drugs or protein interactions, which occur over temporal scales ranging from milliseconds to seconds. Traditional MD simulations face challenges in modeling large and complex biological systems because of computational constraints. However, recent advancements have substantially extended their capabilities, allowing the simulation of larger biomolecular systems over longer timescales[49–52]. HS-AFM complements these advancements by enabling high-speed imaging of complex protein surface structures and dynamics and provides detailed insights into their functional activities[53]. NMR can simultaneously resolve the atomic structures and interactional dynamics but remains limited by the protein size, even with recent advancements in in-cell NMR. AFMfit utilizes an iterative fitting process that progressively modifies an input 3D atomic model (e.g., those obtained from a protein data bank, PDB or models from MD simulations) to match the 2D molecular surface images captured from multiple experimental AFM observations. AFMfit mutually explores the rigid and flexible degrees of freedom via the fast Fourier transform (FFT) and the nonlinear rigid block normal-mode analysis (NOLB-NMA) methods, respectively[54–56]. Overcoming the discrepancies in temporal and spatial resolution between the experimental AFM data and simulation data would enable

110 a thorough comparison of these two types of data in dynamic atomic structural
111 biology.
112 In this study, our goal was to explore the atomic conformational dynamics and
113 actin-crosslinking function of alpha-actinin through a multidimensional approach.
114 Thus, we developed an innovative workflow (SimHS-AFMfit) to transform the 2D
115 AFM images into three-dimensional (3D) atomic conformations by integrating HS-
116 AFM with the normal mode-based flexible fitting algorithm AFMfit[57] and MD
117 simulations[40,44–46]; this strategy partially bridges the spatial and temporal gaps
118 between the experimental AFM data and MD simulations. This enabled the
119 interpretation of the HS-AFM data with the 3D atomic models and overcame the
120 limitations of direct visualization techniques. MD simulations have extended our
121 understanding of protein dynamics by capturing atomic structural transitions on the
122 nanosecond timescale, providing complementary insights into molecular flexibility
123 and stability[58].
124 To validate our methodology, we applied it to smooth muscle alpha-actinin, which
125 is a key cytoskeletal protein that plays a crucial role in crosslinking actin filaments
126 and interacts with other regulatory proteins. We examined the atomic structure and
127 conformational changes of alpha-actinin in both the Ca^{2+}-bound and Ca^{2}-unbound
128 states. To expand our understanding of the general role of alpha-actinin in the
129 dynamics and function of muscle, stress fibers, and contractile rings, we applied
130 our methodology to actin filaments crosslinked with and without alpha-actinin.
131 Specifically, we aimed to use our approach to investigate (i) the contribution of
132 alpha-actinin to the spatial organization of the actin filament protomers and their
133 conformational changes and (ii) the interactions between the actin filaments and
134 alpha-actinin and regulatory proteins such as the myosin II head (S1) and cofilin in
135 the unipolar and bipolar crosslinking models.
136 Our SimHS-AFMfit was used to quantify the flexibility and domain motions of
137 alpha-actinin across various conformations, including twisting, bending, and
138 rotation motions in alpha-actinin. HS-AFM and MD simulations were also used to
139 explore the atomic conformations of the actin filaments in unipolar and bipolar

140 crosslinking models and further elucidated the role of alpha-actinin in regulating
141 the binding of S1 and cofilin in solutions containing ATP and with or without Ca^{2+},
142 which mimic the minimal system of sarcomeres, stress fibers, and contractile
143 rings[59–64]. The key findings included the fluctuations in the rise and AD of the actin
144 protomers in unipolar and bipolar crosslinking models, and residue–contact maps
145 were attained. Ultimately, we aimed to improve our understanding of the biological
146 roles of alpha-actinin and actin filament in muscle, stress fibers, contractile rings,
147 and focal adhesions, including their functions in unipolar and bipolar crosslinking
148 models; their physical impacts when interacting with actin regulatory proteins such
149 as cofilin and myosin II; and their contributions to cellular mechanics, with broader
150 implications for cytoskeletal research.
151

152 **Results**

153 **Overview of the methodology for integrating HS-AFM with AFMfit and MD**
154 **simulations**

155 The focus of this study was to understand how proteins change their atomic
156 structure and how these conformational changes are related to their functions.
157 Equally crucial, however, is understanding the protein dynamics, such as folding
158 and interaction processes since these processes directly influence the biological
159 roles of proteins. HS-AFM can provide insights into the dynamic structural changes
160 in proteins during their functional processes in solution[53,65,66]. While it has high
161 temporal resolution, HS-AFM lacks the atomic spatial resolution of cryo-electron
162 microscopy (cryo-EM). Therefore, one of the major challenges with AFM lies in
163 interpreting its low-resolution, 2D surface images into detailed 3D atomic
164 conformations.
165 The innovative aspect of this research lies in the combination of three methods:
166 HS-AFM, AFMfit (a method for fitting AFM images), and MD simulations to create
167 SimHS-AFMfit (**Fig. 1A-C**). By integrating these techniques, we can achieve a
168 more comprehensive view of the 3D atomic structure of proteins and their dynamic
169 changes during their functional activities.

170 Our methodology was used to analyze the conformational changes in the Ca^{2+}-
171 bound and Ca^{2+}-unbound alpha-actinin over milliseconds to seconds and to
172 determine the atomic conformational dynamics of this protein. Alpha-actinin is an
173 antiparallel homodimer with a molecular weight exceeding 200 kDa. In the domain
174 composition and structure of chicken gizzard smooth muscle alpha-actinin (PDB:
175 1SJJ)[6], alpha-actinin consist of the following: an N-terminal actin binding domain
176 (ABD), in which the two calponin homology 1 and 2 (CH1, CH2) domains are in
177 extensive contact; a central region containing four spectrin-like repeat (SR1-SR4)
178 or rod domains; and a C-terminal calmodulin-like domain (CaMD) that includes two
179 pairs of EF-hand motifs (EF12 and EF34), and the EF12 domain is responsible for
180 Ca^{2+} binding. The two ABDs undergo a 90-degree rotation, enabling alpha-actinin
181 to crosslink the actin filaments in nearly any orientation[6] (**Fig. 1A, B**).
182 We used SimHS-AFMfit to generate libraries of atomic models in different
183 conformations for both Ca^{2+}-bound and Ca^{2+}-unbound alpha-actinin through a
184 workflow (**Fig. 1C**); this provided insights into their atomic structures and collective
185 motions over time. First, alpha-actinin molecules were gently immobilized on mica,
186 and AFM data were collected with a typical imaging rate of 100 ms per frame. We
187 then processed the HS-AFM Supplementary Videos with AFMfit, starting with a
188 reference atomic model derived from the MD simulations. Specifically, AFMfit fit
189 this reference model to the experimental AFM data by generating pseudo-AFM
190 images derived from this reference model over two fitting steps. The first step was
191 a rigid fitting step in which the reference model was rigidly aligned with the AFM
192 experimental data to obtain an optimal pose using an exhaustive search algorithm
193 based on the FFT. In the second flexible fitting step, the aligned models were
194 flexibly deformed using the NOLB technique[54] to obtain the optimal elastic
195 alignment of the atomic models to multiple AFM observations. By applying this
196 iterative process to our alpha-actinin AFM data, we obtained the corresponding
197 conformational libraries for the protein (see the Supplementary Methods).
198 Simultaneously, the same initial protein model (PDB: 1SJJ)[6] was used as the
199 starting point for the MD simulations (see the Supplementary Methods); these were

200 conducted over a timescale of 500 nanoseconds and similarly produced a set of
201 conformation libraries for alpha-actinin.
202 Both the AFMfit and MD simulation-based atomic conformations were then
203 analyzed with principal component analysis (PCA); this enabled the interpretation
204 of these conformational ensembles as the conformational dynamics of the atomic
205 structure of the protein, surpassing X-ray scattering and cryo-EM methods.

206 **Ca^{2+} binding affects smooth muscle alpha-actinin length flexibility**

207 First, we employed state-of-the-art HS-AFM to obtain high spatiotemporal
208 resolution images of alpha-actinin. Two-dimensional molecular surface images of
209 the individual Ca^{2+}-bound and Ca^{2+}-unbound alpha-actinin molecules on mica
210 were continuously recorded under near-physiological conditions at an imaging rate
211 of 100 ms per frame (**Fig. 1D, Supplementary Video 1**). To distinguish the
212 conformational dynamics between these two states, we tracked the positions (x, y,
213 and z coordinates) of the two ABD spheres on opposite sides of multiple alpha-
214 actinin molecules over sequential frames and calculated the distance between
215 their peak heights (Pseudo AFM alpha-actinin-PDB: 1SJJ in **Fig. 1B**). HS-AFM
216 revealed that the length flexibility of alpha-actinin decreased in the presence of
217 Ca^{2+} compared with its absence. From the 2D HS-AFM dataset, the mean ± SD
218 heights and lengths were 6.3 ± 0.9 nm (N = 7236) and 25.2 ± 2.3 nm (N = 3516)
219 for Ca^{2+}-bound alpha-actinin and 5.5 ± 0.8 nm (N = 4043) and 25.6 ± 3.6 nm (N =
220 2016) for Ca^{2+}-unbound alpha-actinin. The results revealed statistically significant
221 differences ($p < 0.05$) in the height and length distributions between the Ca^{2+}-
222 bound and Ca^{2+}-unbound alpha-actinin (**Fig. 1E**).
223 The HS-AFM data in **Fig. 1E** were compared with those obtained by the AFMfit
224 and MD simulations (**Fig. 1F, Supplementary Table 1**). From the 3D AFMfit
225 dataset, the lengths were 24.7 ± 0.9 nm (N = 1466) for Ca^{2+}-bound and 25.2 ± 1.4
226 nm (N = 1140) for Ca^{2+}-unbound alpha-actinin. Similarly, in the 3D MD simulation
227 dataset, the corresponding values were 25.4 ± 0.6 nm (N = 500) for the Ca^{2+}-bound
228 alpha-actinin and 24.1 ± 0.7 nm (N = 500) for the unbound alpha-actinin (**Fig. 1F**).
229 Specifically, the Ca^{2+}-bound state yielded a narrower distribution of length,

230 indicating that the binding of Ca^{2+} to the EF12 domain constrained the molecular
231 dynamics of alpha-actinin. The length distributions obtained from the AFMfit and
232 MD simulations were noticeably similar (**Fig. 1F**); these results supported the
233 reliability of SimHS-AFMfit, despite their narrower distributions when compared
234 directly with the 2D HS-AFM data (**Fig. 1E**).

235 **HS-AFM analysis of the structures of the unipolar actin filaments crosslinked**
236 **with alpha-actinin in the presence or absence of S1 or cofilin**

237 Having demonstrated the positional distributions of alpha-actinin in the bound and
238 unbound states with Ca^{2+}, we next employed HS-AFM to capture the changes in
239 the structure of the unipolar crosslinking model in the presence of S1, ATP, and
240 $CaCl_2$ (**Fig. 2, Supplementary Fig. 1, Supplementary Video 2**). The unipolar
241 crosslinking configuration, in which the actin filaments shared the same polarity
242 (**Supplementary Table 1**), was identified by examining the persistent binding of
243 S1 to the actin filaments; the persistent binding occurred when ATP was gradually
244 depleted and was explained in captions **Supplementary Fig. 1B** and
245 **Supplementary Video 2**[3,22,67]. Our semiautomatic method was previously
246 developed to precisely measure the half-helical pitch (HHP), the number of
247 protomer pairs per HHP, and the mean axial distance (MAD) between the adjacent
248 protomers along the same long-pitch strand[24] and was employed for these
249 analyses (**Fig. 2A, Supplementary Fig. 1A**). These parameters changed over
250 time (**Fig. 2B, Supplementary Fig. 1C**), indicating that HHP, the number of actin
251 protomer pairs per HHP, and the MAD values of actin filaments in the unipolar
252 crosslinking configuration in the presence of ATP and S1 were not static but rather
253 dynamic. Consequently, these parameters were characterized by broad
254 distributions: HHP (36.3 ± 2.3 nm, N = 1055); number of protomer pairs per HHP
255 (5.5 pairs/HHP [5.4%], 6.5 pairs/HHP [80.3%], 7.5 pairs/HHP [13.8%], and 8.5
256 pairs/HHP [0.5%], N = 6956.5); and MAD (5.5 ± 0.3 nm, N = 1055) (**Fig. 2C**). In
257 the presence of ATP but not S1, the mean HHP in the filaments crosslinked by
258 alpha-actinin was 36.5 ± 2.8 nm (N = 4270) (**Supplementary Fig. 1D, E,**
259 **Supplementary Video 3**); these results were similar to those observed in the

260 presence of both S1 and ATP (**Fig. 2C**). These results indicated that the HHP of
261 the actin filaments in unipolar crosslinking models underwent intrinsic thermal
262 fluctuations around a mean value, driven by changes in the number of protomer
263 pairs per HHP and MAD. Under ATP-nearly depleted conditions, S1 persistently
264 associated with the actin filaments in these unipolar crosslinking models
265 (**Supplementary Fig. 1B, Supplementary Video 2**).

266 **Alpha-actinin inhibits the shortening of major pitch and cofilin binding and**
267 **the formation of mature cofilin clusters**

268 The HHP and MAD values obtained in this study (**Fig. 2, Supplementary Fig. 1,**
269 **Supplementary Videos 2, 3**) were compared with those of the control actin
270 filaments (specifically, those without alpha-actinin crosslinking) investigated in our
271 previous studies (e.g., HHP: 36.8 ± 4.3 nm, MAD: 4.3–5.6 nm)[22,24]; here, the
272 physical mechanisms by which crosslinking with alpha-actinin affected the helical
273 twists of the actin filaments upon interaction with S1 or with no S1 interaction were
274 further investigated.

275 To further explore the physical effects of alpha-actinin on the helical twists of the
276 actin filaments, we initially induced crosslinking between the actin filaments and
277 alpha-actinin in the presence of ATP and $MgCl_2$. Cofilin was then added at a final
278 concentration of 600 nM; this concentration was significantly greater than its
279 binding affinity (k_d) of 5–10 nM for bare actin filaments[68], and the results were
280 compared with those of the actin filaments with cofilin but without the alpha-actin
281 crosslinking (**Fig. 3A-C, Supplementary Table 1, Supplementary Video 4**). The
282 kinetics of the peak height and HHP fluctuations were analyzed using the same
283 approach as in our previous studies[22,24] (**Fig. 3A, B**). In our experiments, the
284 crosslinked filaments were arranged with the same polarity, as determined by the
285 similar crosslinking angles of alpha-actinin[3]. The mean peak height and HHP
286 values of the actin segments crosslinked with alpha-actinin and bound with cofilin
287 (cofilactin-actinin clusters) were 9.9 ± 1.1 nm (N = 2514) and 33.0 ± 4.6 nm (N =
288 2003), respectively; however, the corresponding values of the mature cofilactin
289 clusters without alpha-actinin crosslinking, which served as the control, were

290 significantly different ($p < 0.05$), with values of 10.7 ± 1.0 nm (N = 425) and 29.7 ±
291 3.0 nm (N = 300), respectively (**Fig. 3C, Supplementary Table 1**). Two key
292 findings emerged from these experiments: (i) Alpha-actinin significantly inhibited
293 the super twisting of the half helices. Specifically, the major pitches of the half
294 helices of the actin segments crosslinked by alpha-actinin were unable to undergo
295 the shortening induced by the immature cofilactin-actinin clusters; this was
296 reflected by their greater HHP values relative to those of the mature cofilactin
297 clusters without the alpha-actinin crosslinking (HHP: 33.0 ± 4.6 nm vs. 29.7 ± 3.0
298 nm). (ii) Alpha-actinin strongly inhibited the cofilin binding and the formation of the
299 mature cofilin clusters since the peak height of immature clusters of cofilactin-
300 actinin (9.9 ± 1.1 nm) was significantly lower ($p < 0.05$) than that of the mature
301 cofilactin clusters (10.7 ± 1.0 nm) (**Supplementary Table 1**); however, these
302 values were significantly greater ($p < 0.05$) than that of the bare actin segments
303 (8.6 ± 0.8 nm), as identified in our previous study[22].

304 **Myosin II and cofilin competitively bind to long and short half helices to**
305 **facilitate cluster formation**

306 The debate on how the actin filaments adopted different conformations to regulate
307 the functions and localizations of various actin-binding proteins (ABPs) within cells
308 is ongoing[17]. To further address this issue, HS-AFM was used to observe the
309 competitive binding of S1 and cofilin to the actin filaments in a buffer containing
310 ADP and ATP. The actin filaments were gently immobilized on a lipid membrane
311 in F-buffer initially containing 1 mM ADP, 0.01 mM ATP, 0.5 mM $MgCl_2$ and 300
312 nM S1, followed by the addition of 100 nM cofilin (**Fig. 3D-F, Supplementary Fig.**
313 **2, Supplementary Videos 5, 6**). Under high-ADP and low-ATP conditions, S1
314 transiently associated with the actin filaments and dissociated from the actin
315 filaments, whereas cofilin actively sought binding sites to form clusters. The
316 transient interaction of S1 with the actin filaments consumed ATP, and since ATP
317 became depleted, stable S1 clusters formed; however, these S1 clusters were
318 spatially segregated from the cofilin clusters on the same actin filaments. Analysis
319 of the peak heights and HHPs in the mature S1-actin and cofilactin segment

320 clusters (**Fig. 3D**) revealed that the S1 clusters (14.9 ± 1.4 nm (N = 1051) and 33.9
321 ± 4.4 nm (N = 805)) contained higher and longer HHPs than the cofilin clusters
322 (10.5 ± 1.0 nm (N = 935) and 25.7 ± 3.6 nm (N = 767)), as assessed by the
323 statistical significance ($p < 0.05$) (**Fig. 3E, F, Supplementary Table 1**). These
324 findings indicated that S1 and cofilin preferentially bound long and short half
325 helices, respectively, when their stable clusters were formed. Interestingly, these
326 clusters remained segregated on the same actin filaments under ATP-depleted
327 conditions, likely because long HHPs, which supported stable S1 binding; these
328 represented stable half helices similar to those in well-defined or canonical actin
329 filaments, whereas the shorter HHPs, which accommodated the cofilin clusters,
330 corresponded to the constrained and less stable half helices. However, the specific
331 features of the actin filaments that governed the accommodation of S1 and cofilin
332 before and after ATP depletion remained elusive when only HS-AFM, which is a
333 technique that provided the 2D surface structures with nanometer and millisecond
334 resolution, was used. Further exploration of the structural differences among the
335 actin filaments of the different configurations, such as the degree of helical twisting,
336 the number of protomer pairs per HHP, the rise, and the ADs, was crucial for
337 understanding how these properties regulated the binding and functions of
338 different ABPs.

339 **Investigating alpha-actinin dynamics at the atomic level via SimHS-AFMfit**
340 Our HS-AFM–based analyses helped elucidate some of the characteristics of
341 alpha-actinin, including its fluctuations in height and length over time, as well as its
342 actin-crosslinking functions. However, these conventional AFM analyses were
343 unable to reveal the critical insights into the conformational dynamics of the atomic
344 structure and domain interactions of alpha-actin, such as its bending, rotation, and
345 twisting motions. An understanding of these dynamics is essential for
346 understanding the mechanical influence of alpha-actinin on the structure,
347 dynamics, and function of the actin filaments. Thus, we created SimHS-AFMfit
348 through the integration of HS-AFM with AFMfit and MD simulations to further
349 explore the dynamics and atomic structure of alpha-actinin. We employed AFMfit
350 to convert the 2D molecular surfaces of alpha-actinin obtained from HS-AFM into
351 3D atomic conformations (**Fig. 4, Supplementary Fig. 3A, B, Supplementary**
352 **Videos 7, 8**). Using this approach, we generated libraries of the conformations for
353 the Ca^{2+}-bound and Ca^{2+}-unbound alpha-actinin (**Fig. 4A**). These conformations
354 were subsequently aligned to compare the dynamics of the two states according
355 to both the AFMfit analyses and the MD simulations. The distribution of the
356 positions of Cα was broader in the AFMfit analyses than in the MD simulations
357 (**Fig. 4A**); this likely occurred because the 100-millisecond-scale HS-AFM
358 measurements captured more extensive molecular movements than the 0.5-
359 microsecond MD simulations. Additionally, substrate interactions that occurred
360 during the AFM analysis, which were not present in the MD simulation results,
361 could influence the dynamics of alpha-actinin.
362 The root mean square fluctuation (RMSF), which is a commonly used metric for
363 evaluating the flexibility and mobility of atoms or residues in proteins, was
364 employed to quantify the deviation of each Cα atom from its average position using
365 the conformational libraries generated with the AFMfit and MD simulations (**Fig.**
366 **4B**). The results revealed the dynamic motions of CH1-CH2 within the ABD, neck,
367 and EF12-EF34 domains, whereas the rod (SR1-SR4) domains exhibited relatively
368 high rigidity. Despite the differences estimated in the fluctuation magnitude, both

369 the AFMfit and the MD simulation results consistently demonstrated that compared
370 with the unbound state, the Ca^{2+} binding significantly reduced the motion of the
371 CH1-CH2 and EF12-EF34 domains near the neck.
372 Next, we quantitatively analyzed the dynamic movements of the individual domains
373 at the atomic level by focusing on the distances between CH1 and CH2 within the
374 ABD and between EF12 and EF34 within the CaMD (**Supplementary Fig. 3C-F,**
375 **Supplementary Table 1**). On the basis of this analysis, the domain distances were
376 classified as either rigid or flexible. For rigid domains with minimal distance
377 fluctuations, AFMfit confirmed that the ABD had the smallest conformation, and
378 the CH1–CH2 distances for the Ca^{2+}-bound and Ca^{2+}-unbound states were 2.45 ±
379 0.01 nm and 2.46 ± 0.01 nm, respectively, and these values were consistent with
380 those from previous structural studies[5] (**Supplementary Fig. 3C-D**). Similarly, for
381 the Ca^{2+}-bound and Ca^{2+}-unbound states, the CH1–EF34 distances were 3.06 ±
382 0.01 nm and 3.07 ± 0.02 nm, respectively, whereas the CH2–EF34 distances were
383 3.63 ± 0.01 nm and 3.63 ± 0.02 nm, respectively. For flexible domains with larger
384 distance fluctuations, AFMfit demonstrated that Ca^{2+} binding significantly reduced
385 the magnitude of fluctuations relative to the unbound state. Specifically, the CH1-
386 EF12 distances were 3.89 ± 0.16 nm and 3.76 ± 0.21 nm for the Ca^{2+}-bound and
387 Ca^{2+}-unbound states, respectively. Similarly, the CH2–EF12 distances were 4.58
388 ± 0.06 nm and 4.53 ± 0.09 nm, whereas the EF12–EF34 distances were 2.81 ±
389 0.05 nm and 2.73 ± 0.07 nm, respectively.
390 The results from the MD simulations corroborated the molecular dynamics of Ca^{2+}-
391 bound and Ca^{2+}-unbound alpha-actin obtained with AFMfit, revealing similar trends
392 at the atomic level (**Supplementary Fig. 3E-F, Supplementary Table 1**). While
393 the AFMfit had greater magnitudes of the domain fluctuations than MD simulations,
394 both methods consistently demonstrated that the Ca^{2+} binding to the EF12 domain
395 reduced the degree of fluctuations in the alpha-actinin dynamics. Our SimHS-
396 AFMfit simultaneously captured and described the atomic conformations and
397 dynamics of alpha-actinin, partially bridging temporal and spatial gaps between the
398 experimental AFM data and MD simulations. This approach surpassed the

399 limitations of previous static structural studies based on X-ray scattering[5,7–9] and
400 cryo-EM[6].

401 **Classifying the dynamic conformations of alpha-actinin via PCA**

402 PCA is a statistical method used to reduce the dimensionality of a dataset while
403 retaining its most significant variations. It is highly effective in identifying and
404 classifying the collective motions of individual protein domains using principal
405 components (PCs).

406 First, we determined the ensemble of the atomic motions of the Ca^{2+}-bound and
407 Ca^{2+}-unbound alpha-actinin by analyzing the libraries of the conformations
408 obtained from both the AFMfit and MD simulations and projected these motions
409 onto a common PCA space (**Fig. 4C, Supplementary Videos 9-11**). The
410 eigenvalues of principal component 1 (PC1), PC2, and PC3 were used to
411 determine the percentage contribution of each motion. PC1 (36%) primarily
412 captured the ensemble of the opposite-direction bending motions or neck rotation,
413 PC2 (20%) represented same-direction bending motions or neck bending, and
414 PC3 (15%) described a combination of opposite-direction bending and twisting
415 motions.

416 To compare the data obtained from the AFMfit and MD simulations, we projected
417 the conformational libraries of the Ca^{2+}-bound and Ca^{2+}-unbound alpha-actinin
418 generated from both the AFMfit analyses and MD simulations onto a common PCA
419 space and plotted the distributions of PC1 versus PC2 and PC1 versus PC3 (**Fig.
420 4D**). For the Ca^{2+}-bound state, PC1 from the AFMfit conformational libraries
421 captured a broad and symmetric distribution of opposite-direction bending,
422 whereas that from the MD simulation libraries demonstrated a narrower and more
423 asymmetric distribution. In contrast, for the Ca^{2+}-unbound state, PC1 from the
424 AFMfit libraries exhibited an asymmetric distribution, whereas that of the MD
425 simulation libraries demonstrated a more symmetric pattern; these results
426 highlighted the different spectral characteristics between the two methods.

427 Despite the differences in the fluctuation magnitude exhibited between the AFMfit
428 analyses and MD simulations (**Fig. 4A-B**), the PC2 value derived from both the

429 AFMfit analyses and MD simulations consistently captured the motions of both the
430 Ca^{2+}-bound and the Ca^{2+}-unbound states; these results indicated the overlapping
431 spectra between the two methods. A similar trend was observed for PC3, which
432 captured comparable fluctuation spectra in the Ca^{2+}-bound state for both methods.
433 However, for the Ca^{2+}-unbound state, PC3 exhibited distinct fluctuation spectra
434 between the two approaches. Therefore, PCA successfully analyzed and
435 categorized the physical motions in the Ca^{2+}-bound and Ca^{2+}-unbound alpha-
436 actinin using PC1, PC2, and PC3; these PCs were derived from the conformations
437 generated via AFMfit analysis and the MD simulations (**Fig. 4**). Across all results,
438 the eigenvectors represented by the white arrows in SR1 and SR4 were small,
439 whereas those in SR2 and SR3 showed almost no motion; these results confirmed
440 the rigidity of the rod domain. In contrast, prominent eigenvectors were observed
441 in CH1–CH2 within the ABD, in EF12–EF34, and in the neck domain, indicating
442 relatively high flexibility in these regions (**Fig. 4A, C**). In summary, our SimHS-
443 AFMfit demonstrates an outstanding ability to capture and categorize the atomic
444 conformational dynamics of the Ca^{2+}-bound and Ca^{2+}-unbound alpha-actinin.
445 To better capture the collective motions of the molecules, we also analyzed the
446 bending and twisting angles of the ABD relative to the rod domain in both the Ca^{2+}-
447 bound and Ca^{2+}-unbound alpha-actinin. As described above, PCA of the
448 conformations confirmed the rigidity of the rod domain (SR2-SR3). With reference
449 to a vector defined along the Cα positions within the SR2-SR3 domain
450 (**Supplementary Fig. 4**), the bending angles were measured relative to the center
451 of mass of the Cα atoms in the CH1, CH2, EF12, and EF34 domains near the neck
452 in chain 1 (red) and chain 2 (blue) (**Supplementary Fig. 4A**). To measure the
453 twisting angles, the vectors were defined by linking the centers of mass of the Cα
454 atoms between the EF12-EF34 and CH1-CH2 domains, and the angles of these
455 vectors were measured relative to the SR2-SR3-aligned reference vector
456 (**Supplementary Fig. 4B**). The distributions of bending and twisting angles in
457 chain 1 and chain 2, with and without Ca^{2+} binding, were analyzed to more
458 effectively capture the directions of the collective motions, whether in the same or

459 opposite direction. Quantitative measurements of the bending and twisting angles
460 in chains 1 and 2 of the Ca^{2+}-bound and Ca^{2+}-unbound alpha-actinin based on the
461 AFMfit and MD simulations (**Supplementary Fig. 4, Supplementary Table 1**)
462 confirmed the flexibility of the bending and twisting motions of alpha-actinin.
463 Despite the previously identified differences between the two methods in their
464 ability to estimate the magnitudes of fluctuation, both the AFMfit and the MD
465 simulations showed that Ca^{2+} binding could restrict these motions to some extent.
466 Our approach effectively refined and categorized the impact of Ca^{2+} on physical
467 motions, such as the bending and twisting of smooth muscle alpha-actinin. When
468 the ensemble of conformations obtained using our method was compared with
469 those obtained from other techniques, such as cryo-EM[6], which reported that
470 isoform 2 alpha-actinin was not sensitive to Ca^{2+}, our findings were not only
471 consistent but also provided a better description of its dynamic nature.

472 **Comparing the key principal components derived from the AFMfit and MD**
473 **simulations**

474 To explore the collective motions of alpha-actinin using a multidimensional
475 approach such as SimHS-AFMfit, we separately projected the conformational
476 libraries of the Ca^{2+}-bound and Ca^{2+}-unbound alpha-actinin generated from the
477 AFMfit analyses and MD simulations onto PCA spaces. We then plotted and
478 compared the key PCs (PC1, PC2, and PC3) that described the collective motions
479 of the domains of alpha-actinin via the same eigenvectors (**Supplementary Fig.**
480 **5, 6, Supplementary Videos 12-15**).

481 For the conformation libraries derived with AFMfit (**Supplementary Fig. 5A,**
482 **Supplementary Videos 12, 13**), PC1, PC2, and PC3 characterized the physical
483 motions of Ca^{2+}-bound alpha-actinin as opposite-direction bending (neck rotation),
484 twisting, and opposite-direction bending (neck rotation), respectively. In contrast,
485 for Ca^{2+}-unbound alpha-actinin, PC1, PC2, and PC3 corresponded to opposite-
486 direction bending (neck rotation), same-direction bending (neck bending), and
487 opposite-direction bending (neck rotation), respectively.

488 Similarly, for the MD simulation-based libraries (**Supplementary Fig. 5B,**
489 **Supplementary Videos 14-15**), PC1, PC2, and PC3 characterized same-direction
490 bending (neck bending), opposite-direction bending (neck rotation), and a
491 combination of twisting and rotation, respectively, in the Ca^{2+}-bound alpha-actinin.
492 In the unbound state, these PCs corresponded to same-direction bending (neck
493 bending), opposite-direction bending (neck rotation), and twisting, respectively.
494 Based on the eigenvectors derived from the conformation libraries obtained with
495 AFMfit for both the bound and unbound states (**Supplementary Fig. 5A, B**), PC1
496 and PC3 consistently captured the opposite-direction bending motions or neck
497 rotations, despite the differences in the fluctuation magnitudes between the AFMfit
498 and MD simulations; these results indicated a high degree of spectral overlap in
499 the conformations derived with the two methods. However, PC2 exhibited distinct
500 behaviors between the states and captured the twisting motions in the Ca^{2+}-bound
501 state and same-direction bending motions or neck rotations in the Ca^{2+}-unbound
502 state, highlighting a significant spectral difference between the two methods.
503 Similarly, based on eigenvectors derived from the conformation libraries obtained
504 from the MD simulations for both the bound and unbound states (**Supplementary**
505 **Fig. 5C, D**), PC1 and PC2 consistently captured the same-direction and opposite-
506 direction bending motions in the Ca^{2+}-bound and unbound states, respectively,
507 despite the differences in the fluctuation magnitudes between the AFMfit and MD
508 simulations; these results further indicated strong spectral overlap. In contrast,
509 PC3 showed distinct behaviors for the two states and captured a combination of
510 twisting and bending motions in the Ca^{2+}-bound state and primarily twisting
511 motions in the Ca^{2+}-unbound state; these results indicated that the two methods
512 revealed significant spectral differences. In summary, SimHS-AFMfit could
513 effectively capture and classify the physical motions of alpha-actinin within various
514 common PCA spaces.
515 The interpretation was further validated by separately analyzing the correlations
516 among PC1, PC2, and PC3 and the bending and twisting angles in chains 1 and
517 2 (**Supplementary Fig. 7, 8, Supplementary Videos 12-15**). In both the Ca^{2+}-

518 bound and Ca^{2+}-unbound states derived from AFMfit, PC1 and PC3 demonstrated
519 strong positive and negative linear correlations with the bending angles of the two
520 chains (**Supplementary Fig. 7**); these results confirmed opposite-direction
521 bending between them (**Supplementary Fig. 5A, Supplementary Videos 12-13**).
522 Conversely, PC2 exhibited a strong linear correlation with the twisting angle in the
523 Ca^{2+}-bound state and confirmed the role of this PC in capturing the twisting motion.
524 However, in the Ca^{2+}-unbound state, the correlations between PC2 and the
525 bending angles for chains 1 and 2 were very similar; these results indicated that
526 this PC captured the same-direction bending motions for this conformation
527 (**Supplementary Fig. 5A, 7B, Supplementary Video 12-13**).
528 In both the Ca^{2+}-bound and Ca^{2+}-unbound states derived from the MD simulations,
529 PC1 exhibited strong negative linear correlations with the bending angles of both
530 chains (**Supplementary Fig. 8**) and indicated the same-direction bending in the
531 two conformations (**Supplementary Fig. 5B, Supplementary Videos 14-15**). In
532 contrast, PC2 demonstrated strong negative and positive linear correlations with
533 the bending angles in the two chains; these results indicated opposite-direction
534 bending in the Ca^{2+}-bound and Ca^{2+}-unbound states, whereas PC3 was weakly
535 correlated with the two bending angles and was largely sensitive to the twisting
536 angle; thus, this PC captured a combination of twisting and bending motions in the
537 Ca^{2+}-bound state and primarily twisting motion in the Ca^{2+}-unbound state
538 (**Supplementary Fig. 5B, 8, Supplementary Videos 14-15**).
539 Overall, the AFMfit and MD simulations consistently identified the key motions in
540 both the Ca^{2+}-bound and Ca^{2+}-unbound alpha-actinin, although some
541 discrepancies remained due to factors such as differences in the temporal and
542 spatial resolutions or sample fixation between the HS-AFM and MD simulations.
543 AFMfit was shown to be a powerful tool for transforming the 2D surface images
544 obtained from AFM into 3D atomic conformations; however, its integration with
545 complimentary techniques such as MD simulations is crucial for addressing the
546 spatial and temporal gaps in the AFM data.

547 **Analyzing complex protein models using SimHS-AFMfit**

548 In this study, we developed a novel strategy that integrated HS-AFM, AFMfit, and
549 MD simulations (SimHS-AFMfit) to address some limitations in the spatial and
550 temporal resolution of AFM using Ca^{2+}-bound and Ca^{2+}-unbound alpha-actinin.
551 This approach successfully captured the physical motions of individual domains
552 and distinguished the atomic conformational changes in alpha-actinin following
553 binding with Ca^{2+}.

554 However, converting complex 2D AFM images of actin filaments crosslinked to
555 alpha-actinin (**Fig. 2, Supplementary Fig. 1, Supplementary Videos 2, 3**) into
556 3D atomic conformations with AFMfit remained challenging because of the intricate
557 nature of these protein assemblies, which include both actin filaments and alpha-
558 actinin. By also employing MD simulations, we constructed two models of unipolar
559 and bipolar crosslinking, along with a model of a bare actin filament, and these
560 models were simulated under the same conditions used for alpha-actinin for 100
561 ns (**Fig. 5, Supplementary Fig. 9, Supplementary Videos 16-20**).

562 We next analyzed the atomic conformational dynamics of Ca^{2+}-unbound alpha-
563 actinin in the unipolar and bipolar models (**Supplementary Fig. 9, Supplementary**
564 **Videos 16-17**). In the unipolar configuration, PC1, PC2, and PC3 primarily
565 captured same-direction (neck bending), opposite-direction (neck rotation), and
566 same-direction (neck bending) motions, respectively, as indicated by the
567 trajectories marked by the white arrows (**Supplementary Fig. 9A, Supplementary**
568 **Video 16**). Conversely, in the bipolar model, PC1, PC2, and PC3 corresponded to
569 opposite-direction (neck rotation), same-direction (neck bending), and an
570 unclassified mode predominantly observed in lower ABD movements, respectively
571 (**Supplementary Fig. 9B, Supplementary Video 17**).

572 Since each actin filament in all the MD simulation models contained 13 fixed
573 protomers (equal to 6.5 promoter pairs/HHP), the fluctuations in the HHP across
574 all conformations were minimal, with values of ~36.2 ± 0.0 nm for bare actin, 36.3
575 ± 0.0 nm for both bipolar-flexible and bipolar-fixed models, and 36.3 ± 0.0 nm for
576 the unipolar-flexible model (**Fig. 5A, C; Supplementary Table 1**). These values

577 aligned with our expectations from previous findings and indicated that the
578 fluctuations in the HHP primarily resulted from the variations in the number of
579 protomers per HHP[24,25,69]. However, the rise values exhibited large fluctuations of
580 varying magnitudes: 2.8 ± 0.1 nm for bare actin, 2.8 ± 0.2 nm and 2.9 ± 0.2 nm for
581 the bipolar-flexible and bipolar-fixed models, respectively, and 2.8 ± 0.1 nm for the
582 unipolar-flexible model. A similar trend was observed in the AD values, with values
583 of 5.6 ± 0.1 nm for bare actin, 5.7 ± 0.2 nm for both bipolar-flexible and bipolar-
584 fixed models, and especially 6.0 ± 0.3 nm for the unipolar-flexible model (**Fig. 5C,**
585 **Supplementary Table 1**). Statistical analysis revealed that when comparing the
586 bare actin filaments to those in the unipolar and bipolar models, the AD values
587 were significantly different ($p < 0.05$, *t-test*), whereas the rise values were not
588 significantly different (**Fig. 5C, Supplementary Table 1**). Additionally, the rise
589 values between the bipolar-fixed model and that in bipolar-flexible and unipolar-
590 flexible models were also significantly different ($p < 0.05$, *t-test*), whereas the rise
591 and AD values were not significantly different when comparing them between
592 bipolar-flexible and unipolar-flexible models.
593 The local residue contact maps between the two ABDs in the alpha-actinin
594 molecule and the actin protomers greatly differed between the unipolar-flexible and
595 bipolar-flexible and bipolar-fixed crosslinking models (**Fig. 5D, E; Supplementary**
596 **Table 1**). These differences provide a biochemical basis for validating key
597 component interactions that regulate conformational changes in actin filaments
598 across different cellular assemblies.
599 These findings indicated that the fluctuations in rise and AD were intrinsic
600 properties of actin filaments and that binding with alpha-actinin further amplified
601 the AD fluctuations compared with those of bare filaments. The binding of alpha-
602 actinin to actin filaments differed between the unipolar and bipolar models in
603 several aspects, including the residue-level interactions between the alpha-
604 actinin's ABDs and actin filaments, the spacing between the two filaments, and the
605 crosslinking angles of alpha-actinin relative to the filaments (**Fig. 5,**
606 **Supplementary Fig. 10, Supplementary Table 1**). Consequently, alpha-actinin

607 could exert distinct physical effects, such as neck bending or neck rotation
608 (**Supplementary Fig. 9**), on the actin protomers and cause differential
609 conformational changes, as reflected in the significantly increased AD fluctuations.
610 This prediction was validated by the MD simulations of bipolar-fixed model, which
611 revealed restricted motion of alpha-actinin (**Fig. 5, Supplementary Video 20**). This
612 restriction is unlikely to influence the increased fluctuations in rise and AD of
613 filaments, suggesting that alpha-actinin's ABD binding alone (**Supplementary**
614 **Table 1**) is sufficient to drive these changes.

615 **Discussion**

616 **Alpha-actinin regulates the dynamic conformations and functions of the**
617 **actin filaments by interacting with myosin II while inhibiting cofilin binding**
618 **and cluster formation**

619 In this study, we successfully developed a novel workflow, SimHS-AFM, to convert
620 the 2D AFM images of alpha-actinin (**Fig. 1, Supplementary Video 1**) into the 3D
621 atomic conformations. This workflow enables the classification of the physical
622 motions of these proteins through PCA (**Fig. 4, Supplementary Videos 7-15**),
623 including their domain distances and twisting and bending modes
624 (**Supplementary Fig. 3-8, Supplementary Videos 12-15**). We further explored
625 the roles of Ca^{2+} in regulating the conformational changes of smooth muscle alpha-
626 actinin and simulate its actin-crosslinking effects on the dynamics and atomic
627 structure of the actin filaments (**Fig. 5, Supplementary Fig. 9, Supplementary**
628 **Videos 16-17**). Additionally, we identify the variations in rise and AD,
629 distinguishing the bare actin filaments (2.8 ± 0.1 nm, 5.6 ± 0.1 nm) from their
630 unipolar (2.8 ± 0.1 nm; 6.0 ± 0.3 nm) and bipolar (2.8 ± 0.2 nm, 5.7 ± 0.2 nm)
631 flexible models (**Fig. 5C, Supplementary Table 1, Supplementary Videos 18-**
632 **19**). These structural characteristics, including the rise and AD fluctuations as well
633 as distinct residue-level interactions, play critical roles in regulating the excitatory
634 binding of myosin II (S1) and the inhibitory binding of cofilin. These findings
635 increase our understanding of the physical properties and biological functions of
636 alpha-actinin and actin filaments.

637 Additionally, we experimentally investigated the actin-crosslinking with alpha-
638 actinin in unipolar configurations using HS-AFM (**Fig. 2, Supplementary Fig. 1,**
639 **Supplementary Videos 2-3**). This led to the hypothesis that alpha-actinin
640 crosslinking increased the rise and AD or MAD fluctuations, which aligned with the
641 MD simulation results, and influenced the binding of S1 and cofilin (**Fig. 6A, Fig.**
642 **3A-C, Supplementary Video 4**).
643 i) Bare actin filaments typically support the normal binding and functional activity
644 of cofilin and S1 (**Fig. 3D-F, Supplementary Fig. 2, Supplementary Videos 5-6**).
645 The binding and clustering of cofilin tend to shorten the HHP by approximately
646 25%, reducing the number of the protomer pairs per HHP (usually to 4.5 or 5.5
647 protomer pairs per HHP)[24,70–72]. In contrast, S1 binding maintains a longer HHP
648 (**Fig. 3D-F, 6A**).
649 (ii) When alpha-actinin crosslinks with the actin filaments in the unipolar model,
650 cofilin binding and the formation of the mature cofilin clusters are substantially
651 inhibited, thus preventing the shortening of the HHP (**Fig. 3B, Supplementary**
652 **Video 4B**). Moreover, alpha-actinin crosslinking preserves a long HHP without
653 affecting the binding activity of S1 (**Fig. 2, 6A, Supplementary Fig. 1,**
654 **Supplementary Videos 2-3**).
655 Our findings indicate that the fluctuations in rise and AD are inherent in the bare
656 actin filaments and that crosslinking with alpha-actinin further strengthens the AD
657 vibrations in both the bipolar and unipolar models. Interestingly, even when all Cα
658 atoms in alpha-actinin were computationally constrained while the other atoms
659 remained flexible, the MD simulations of a bipolar model over 100 ns (**Fig. 5C**)
660 reveal that ABD binding to actin filaments alone is sufficient to drive these
661 enhanced structural changes. Residue-level contacts play a crucial role in
662 determining the extent of the AD fluctuations (**Fig. 5D-E, Supplementary Table**
663 **1, Supplementary Videos 19-20**). These results are further supported by our MD
664 simulations, which demonstrate that allowing backbone inflexibility in the Cα atoms
665 of alpha-actinin in the bipolar-fixed crosslinking model result in AD values
666 comparable to those observed in the fully flexible alpha-actinin model, where

667 rotational motions of the ABD around the neck or just strong alpha-actinin's ABD-
668 actin electrostatic interaction enhance the AD fluctuations in the actin filaments.
669 Notably, previous experimental data have demonstrated that fluctuations in the
670 rise are more pronounced in the bent actin filaments bound to ADP than in those
671 bound to ADP+Pi[73]. Additionally, the mean axial distance (MAD) between two
672 adjacent actin protomers along the same long-pitch strand is greater within the
673 shortened bare half helices (5.0–6.3 nm) than within the typically sized helices
674 (4.3–5.6 nm)[24]. The differences in the fluctuation magnitudes of the AD or MAD
675 induced by the different ABPs, such as alpha-actinin and cofilin, may provide key
676 insights into how these compounds regulate each other's binding or inhibitory
677 effects on the actin filaments.
678 Interestingly, the actin filaments crosslinked with alpha-actinin play distinct roles
679 depending on their crosslinking configuration and location in a cell (**Fig. 6B**). In the
680 bipolar model, they are involved primarily in structures such as contractile rings
681 (CRs), stress fibers, and sarcomeres, whereas in the unipolar configuration, they
682 contribute to lamellipodia, filopodia, cortical actin, and microvilli (**Supplementary**
683 **Table 2**). Our results indicate that future research should focus on experimentally
684 investigating the atomic conformational dynamics of the actin filaments in unipolar
685 and bipolar crosslinking models, including rise, AD fluctuations, and key residue-
686 interactions (**Supplementary Tables 1-2**), to gain deeper insights into the
687 functional and spatial differences between these assemblies within the cells.

688 **Advantages of SimHS-AFMfit**

689 Time-resolved cryo-EM is emerging as a powerful tool for investigating protein
690 dynamics and atomic conformations simultaneously[74–76]. Its potential can be
691 further enhanced by integrating approaches such as cryo-EM flexible fitting[77] and
692 computational methods. Additionally, advanced NMR spectroscopy provides
693 complementary insights and captures both structural and dynamic aspects of
694 proteins during interactions[42,43,78,79].
695 While NMR spectroscopy excels in studying protein structure, dynamics, and
696 interactions, it has limitations. Traditional solution-state NMR is most effective for

proteins under ~30–50 kDa, although techniques such as transverse relaxation-optimized spectroscopy (TROSY) extend this range to ~100 kDa. Larger proteins suffer from the signal overlap and line broadening because of the slow molecular tumbling and transverse relaxation. Compared with cryo-EM and X-ray crystallography, NMR also has lower sensitivity, and peak overlap complicates resonance assignments in complex systems[43,80–82].

In dynamic studies, NMR provides insights into timescales from picoseconds to seconds but struggles with motions faster than 10 ps or slower than seconds to minutes[81,82]. Solid-state NMR remains challenging for membrane proteins because of the need for extensive isotopic labeling and specialized pulse sequences[82]. Additionally, weak or transient interactions can produce signals that are too faint for accurate characterization. Sample preparation and long data acquisition times (hours to days) further risk protein degradation or aggregation[80]. While cryo-EM surpasses NMR in resolving large protein complexes (>100 kDa), it is less effective for studying dynamics[83]. However, these techniques can complement each other[84]. Other single-molecule techniques, such as FRET, can complement NMR for fast dynamics[85], but no standalone method can perfectly capture the atomic structures, dynamics, and interactions simultaneously.

Despite the inherent limitations of AFM, such as its ability to capture only 2D surface images with a maximum spatial resolution of 1 nm in the x–y plane and 0.1 nm in the z dimension, recent advancements in HS-AFM have significantly increased its temporal resolution. Due to these improvements, imaging at timescales of a few tens of milliseconds or faster can be performed and enable a more precise characterization of protein dynamics[53]. HS-AFM has the ability to image large complex protein systems without the need for chemical labeling, enabling the simultaneous capture of nanostructures, dynamics, and protein interactions or assemblies under near-physiological conditions; this capability surpasses those of NMR and cryo-EM. Additionally, by integrating HS-AFM with the AFMfit[57] and MD simulations[47,48] through SimHS-AFMfit, we generated comprehensive libraries of atomic conformations, facilitating the investigation of

727 the physical motions, atomic structures, and functions of alpha-actinin through
728 PCA and providing a robust framework for improving the interpretation of low-
729 resolution experimental AFM and simulated data. For example, the twisting and
730 bending motions of alpha-actinin were cross-validated through the AFMfit and MD
731 simulations, providing deeper insights into the mechanical effects on the actin
732 filaments. Compared with those of bare actin filaments, the SimHS-AFMfit reveals
733 increased AD dynamic fluctuations in the bare actin filament and bipolar
734 crosslinking models; this capability surpasses previous static structural studies
735 using X-ray diffraction[15,16] and cryo-EM[13,86]. This characteristic of actin filaments,
736 which was originally explored in our previous studies[24] and further demonstrated
737 in various crosslinking models here, may play a crucial role in regulating the
738 binding and function of myosin II, cofilin and other ABPs. Ultimately, this integration
739 addresses the spatial and temporal limitations of experimental AFM data and
740 facilitates the study of the atomic conformational dynamics of more complex
741 protein assemblies.
742 Apparently, SimHS-AFMfit still faces challenges in bridging the temporal gaps
743 between millisecond AFM imaging and microsecond MD simulations, highlighting
744 the need for future improvements to address these discrepancies. Additionally, the
745 ability of AFMfit to fit large complex protein assemblies is still challenging because
746 of the complicated models used, necessitating the development of improved fitting
747 algorithms or models. However, the data obtained through SimHS-AFMfit can be
748 useful for developing force fields to simulate complex protein models, as
749 demonstrated in previous studies[49–52]. Force fields are crucial for accurately
750 validating the interatomic forces acting between the atoms composing the system
751 since they account for the intermolecular or interatomic interactions and energy
752 minimization[87,88]. Specifically, our workflow facilitates the use of AFMfit to analyze
753 the experimental AFM data of complex actin filaments crosslinked with alpha-
754 actinin. More broadly, the conformational libraries could also serve as training data
755 for the deep learning models[89–91] to predict the pseudoatomic structures across
756 different timescales (i.e., prediction of protein dynamics) and help bridge the gap

757 between the experimental and computational methods. In this context, recent
758 advancements in three-dimensional localization AFM (3D-LAFM) have
759 successfully transformed the AFM data into 3D density data[92], facilitating large-
760 scale 3D atomic AFM data generation through the integration with the MD
761 simulations.
762 In conclusion, SimHS-AFMfit provides an innovative approach for overcoming the
763 spatial resolution limitations of AFM data. This method can be further developed,
764 such as by its integration with AI, NMR, cryo-EM, cryo-ET, or in silico AFM[93], to
765 bridge the spatiotemporal resolution gaps between HS-AFM and the MD
766 simulations and to predict protein dynamics; this has enabled real-time studies of
767 the atomic conformational dynamics of complex proteins and surpassing the
768 capabilities of individual techniques. Our approach facilitates new possibilities for
769 advancing the understanding of the atomic structural dynamics of complex protein
770 assemblies that mimic cellular machines.

Methods

Proteins and lipids

Rabbit skeletal actin and human (hs) cofilin 1 were prepared following the same protocol as in our previous study[22]. Chicken gizzard smooth muscle alpha-actinin (isoform 2)[5] was obtained from Cytoskeletons (Sigma, Japan). Subfragment-1 (S1) was prepared from smooth muscle myosin using the method described by Asakasa et al[94].

The lipid compositions used in this study consisted of neutral 1,2-dipalmitoyl-sn-glycero-3-phosphocholine (DPPC, Avanti) and positively charged 1,2-dipalmitoyl-3-trimethylammonium-propane (DPTAP, Avanti). Liposomes were prepared with a DPPC/DPTAP ratio of 90:10 (wt%), and the lipid membrane was subsequently formed on mica[22].

HS-AFM Analysis

We employed high-speed atomic force microscopy (HS-AFM), as previously described[22,24,95], to capture the dynamic conformations of alpha-actinin in various states, providing high-speed imaging and two-dimensional (2D) surface structure of the protein at nanometer resolution. Chicken gizzard smooth muscle alpha-actinin, an isoform 2 (Sigma, Japan), was diluted to 30 nM and imaged in F-buffer containing 20 mM KCl, 10 mM PIPES-KOH (pH 6.8), 0.5 mM $MgCl_2$, 0.25 mM EGTA, 0.25 mM DTT, and 0.5 mM ATP. To observe the dynamic conformational changes in alpha-actinin with $CaCl_2$, the proteins were imaged in the same F-buffer with addition of 0.1-0.2 mM $CaCl_2$.

To investigate the dynamic conformational changes in actin filaments crosslinked solely by alpha-actinin, actin filaments were gently immobilized on a lipid membrane and F-buffer consisting of 0.5 mM $MgCl_2$, 0.5 mM ATP, and 50 nM alpha-actinin, but without $CaCl_2$, was employed for HS-AFM imaging. In all experiments, actin filaments were immobilized on DPPC/DPTAP ratio of 90:10 (wt%) for HS-AFM imaging, as done in our previous study[22].

To study the dynamic conformational changes in actin filaments crosslinked by alpha-actinin in the presence of myosin II heads (S1), actin filaments were

801 gently immobilized on a lipid membrane and immersed in F-buffer containing 1 mM
802 ATP, 0.1 mM $CaCl_2$, 50 nM alpha-actinin, and 1 μM S1, but without $MgCl_2$, for HS-
803 AFM imaging.

804 To study the competitive interactions between cofilin and S1, which utilize
805 distinct short and long helical structures on the same actin filament to form their
806 respective clusters, actin filaments were gently immobilized on a lipid membrane.
807 HS-AFM imaging was performed in an F-buffer initially containing 1 mM ADP, 0.01
808 mM ATP, and 300 nM S1, followed by the addition of 100 nM cofilin.

809 To explore the binding and supertwisting activities of cofilin clusters on the
810 half-helices of actin filaments without and with alpha-actinin crosslinking, actin
811 filaments were gently immobilized on a lipid membrane, either without or with 400
812 nM alpha-actinin crosslinking in F-buffer containing 1 mM ATP, followed by the
813 addition of 600 nM hs cofilin, for HS-AFM imaging.

814 The half helical pitch (HHP), the number of protomer pairs per HHP, and
815 the mean axial distance (MAD) between adjacent actin protomers along the same
816 long-pitch strand within individual HHPs were analyzed for actin filaments
817 crosslinked by alpha-actinin under conditions containing Ca^{2+}, ATP, and S1, but
818 without $MgCl_2$ were analyzed using HS-AFM (**Fig. 2, Supplementary Fig. 1A-C**).
819 The analytical methods used in this study were adapted from our previous
820 research[22,24].

821 ***AFMfit Analysis***

822 AFMfit was originally developed for fitting 3D atomic structures into 2D AFM
823 images[57]. In this study, AFMfit utilized the same PDB files as the initial models
824 used in MD simulations. The models were derived from PDB entry 1SJJ[6] for both
825 Ca^{2+}-bound and Ca^{2+}-unbound states, serving as a reference atomic model.

826 AFMfit started by cropping AFM images into sub-images (referred to as
827 particles) that corresponded to the molecule of interest. This operation was semi-
828 automatic, a first automatic process identifies putative particles using the particle-
829 tracking toolkit TrackPy (Allan, D. B., Caswell, T., Keim, N. C., van der Wel, C. M.,
830 & Verweij, R. W. (2021). soft-matter/trackpy: Trackpy v0.5.0 (v0.5.0). Zenodo.

831 https://doi.org/10.5281/zenodo.4682814), then, we performed a manual double
832 check to remove false positives.

833 The extracted particles were processed with AFMfit. It estimated the optimal
834 rigid and flexible alignments of the model that maximize the similarity between the
835 particles and pseudo-AFM images calculated from the atomic model. The
836 calculation of pseudo-AFM images needed to be adjusted to experimental
837 conditions. Particularly, the shape of the experimental probe tip needed to be
838 estimated to accurately account for the tip-convolution effect. We performed this
839 estimation by an exhaustive search of a smoothness parameter of the pseudo-
840 AFM image calculation over the entire set of particles.

841 AFMfit proceeded in two steps. In the first step, it performed a rigid-body
842 pre-alignment of the model to the particles using an FFT-accelerated 5D
843 exhaustive search that estimated the relative position (two translational degrees of
844 freedom) and orientation (three rotational degrees of freedom) of each particle.
845 The angular step for rotational search was set to 10° and restricted to flat
846 orientations of alpha-actinin to accelerate the computations. The translational step
847 in the z-direction was set to 1 Å.

848 In the second step, it combined the continuous rigid and flexible alignments
849 of the model to the particle using the non-linear normal mode analysis method
850 NOLB[54]. NOLB calculated normal modes using the Rotation-Translation of Blocks
851 (RTB) approximation on an Elastic Network Model (ENM). The interaction cutoff in
852 the ENM is set to 8 Å. We restricted the possible motions of our model to the
853 sixteen lowest frequency normal modes, among which, ten modes were the flexible
854 motions describing the most collective motions of alpha-actinin including bending
855 and twisting. The six normal modes left corresponded to rigid translations and rigid
856 rotations in 3D, which were used to account for continuous rigid rearrangement
857 that could be necessary when flexibly deformating the model. According to the
858 AFMfit method, we iteratively calculated the optimal linear approximation of the
859 normal mode displacement that fitted the particle. Then, we carried out a non-linear
860 extrapolation of the motion following the NOLB methodology. We iterated over the

861 linear approximation and non-linear extrapolation until convergence, which in
862 practice was obtained in five iterations.
863 The flexible fitting procedure balanced between minimizing the deformations
864 toward the initial model (to preserve the structure and avoid unfeasible distortions)
865 and maximized the similarity to the data. This balance was controlled by a
866 hyperparameter λ. We estimated λ with an exhaustive search by performing the
867 flexible fitting over a sample of particles with the objective of allowing a maximum
868 of 10 Å of average root-mean-square deviation (RMSD) toward the initial model.
869 The value of 10 Å was set to roughly adjust to the range of motion typically
870 observed in MD simulations of alpha-actinin. The optimal value was obtained for
871 λ=7.5 (**Supplementary Fig. 3A-B**).
872 ***MD Simulations***
873 Molecular dynamics (MD) simulations were performed to generate libraries
874 of conformations for Ca^{2+}-bound and Ca^{2+}-unbound alpha-actinin and bipolar and
875 unipolar crosslinking models.
876 The initial models for alpha-actinin with and without Ca^{2+} in the bulk system
877 were made from the PDB entry 1SJJ. The alpha-actinin was solvated in a 30 mM
878 KCl solution. The system without Ca^{2+} consists of one alpha-actinin, 182 K^+, 128
879 Cl^-, and 251,756 water molecules. In the system with Ca^{2+}, four K^+ were removed
880 and two Ca^{2+} were placed at the center of C_γ of Asp768 and Asp771. It was
881 confirmed that Ca^{2+} ions are stably bound to Asp residues during the simulation.
882 The histidine residues were assumed to be in the protonation state at pH = 7, since
883 they face the bulk solution. The size of the system was 168.856 × 325.387 ×
884 144.838 $Å^3$. AMBER ff19SB[96], TIP3P[97], the Li and Merz 12-6[98], the Li and Merz
885 12-6-4[99] models were employed for the proteins, water molecules, monovalent
886 ions, and divalent ions, respectively. The system was equilibrated by 1 ns MD
887 simulations with constant temperature (300 K) and pressure conditions (1 bar),
888 followed by 10 ns MD simulations with constant temperature (300 K) and volume
889 conditions. All MD simulations were performed using AMBER22 (D. A. Case, H.
890 M. Aktulga, K. Belfon, I. Y. Ben-Shalom, J. T. Berryman, S. R. Brozell, D. S. Cerutti,

T. E. Cheatham, I. G. A. Cisneros, V. W. D. Cruzeiro, T. A. Darden, N. Forouzesh, G. Giambasу, T. Giese, M. K. Gilson, H. Gohlke, A. W. Goetz, J. Harris, S. Izadi, S. A. Izmailov, et al., AMBER22; University of California: San Francisco, 2022). A Berendsen thermostat[100] was used to control the temperature, and a Monte Carlo barostat with anisotropic scaling was used to control the pressure. The SHAKE algorithm[101] was used to keep the bond length having H atoms constant, enabling the use of a time step of 2 fs. The periodic boundary condition was imposed, and long-range interactions were calculated by the particle mesh Ewald method[102] with a 10 Å cutoff in real space. After the equilibration, the MD simulation was performed for 500 ns with constant temperature at 300 K and volume conditions using the Berendsen thermostat[100]. The trajectories were saved at each 1 ns to generate 500 configuration libraries, which were used to analyse principal component (PC) modes using principal component analysis (PCA) to capture the bending and twisting angles, and distances between domains.

For the unipolar and bipolar systems, two actin fibers crosslinked by an alpha-actinin, the initial coordinates were originally given in the Liu and Taylor' paper[6]. The link in the paper to download the structures is not available now, so a corresponding author, Kenneth A. Taylor, gifted them to us. In the previous calculation using QM/MM[103], water coordination around Mg^{2+} and ADP in the actin protomer was investigated. First, a protomer (PDB code: 8d15)[73] was solvated in a 20 mM NaCl solution with one Mg^{2+} and one ADP. The system consists of one protomer, 73 Na^{+}, 63 Cl^{-}, 1 Mg^{2+}, one ADP, and 23,442 water molecules. For the protein, water molecules, monovalent ions, and divalent ions, the same force fields as in the case of alpha-actinin simulations were used. The Carlson model was employed for ADP[104]. The system was equilibrated by 100 ps MD simulation with constant temperature (300 K) and pressure conditions (1 bar). The actin protomer, ADP, and Mg^{2+} were constrained with a force constant of 10 kcal/mol/$Å^2$ to their original positions. Then, 3 μs MD simulation with constant temperature (300 K) and volume conditions (1 bar) was performed. The actin protomer, ADP, and Mg^{2+} were weakly constrained with a force constant of 0.2 kcal/mol/$Å^2$ to prevent unwanted

921 large structural change in the bulk solution. Water molecules gradually entered the
922 protomer over 2 μs. The coordination of water molecules around Mg^{2+} and ADP
923 was confirmed to be similar to the previous configuration obtained by QM/MM
924 calculation[103]. In the remaining 1 μs simulation, the number of water molecules
925 around Mg^{2+} has fluctuated but did not change. The protomer, ADP, Mg^{2+}, and 27
926 water molecules around Mg^{2+} were picked up and aligned to the Liu and Taylor'
927 configuration by minimizing RMSD between C_α atoms[6]. Then, protomers were
928 elongated while considering the symmetry to form 36 nm fiber, and the fiber in a
929 vacuum while the periodic boundary condition was imposed was minimized to
930 remove bad contacts. In the Liu and Taylor' configuration, a part of the neck
931 domain in the alpha-actinin (residue 251-260) was missing, which was
932 complemented by the Modeller package[105]. The system consisting of two actin
933 fibers and alpha-actinin in a vacuum while the periodic boundary condition was
934 imposed was minimized and then solvated in a 40 mM KCl solution. The final
935 system of unipolar configuration consists of two actin fibers (26 protomers), one
936 alpha-actinin, 1032 K^+, 718 Cl^-, 26 Mg^{2+}, 26 ADP, and 1,433,011 water molecules,
937 and total number of atoms in the system was 4,479,739. The system was shortly
938 optimized with 1000 step minimization and was equilibrated by 130 ps MD
939 simulation with constant temperature (300 K) and pressure conditions (1 bar). The
940 temperature gradually increased up to 300 K. The pressure was anisotropically
941 controlled so that only the box size in z direction was allowed to move, in which
942 the actin fiber was placed along the x direction. During the equilibration, the actin
943 fiber, the alpha-actinin, Mg^{2+}, ADP, and water molecules inside the actin were
944 constrained with a force constant of 2 kcal/mol/$Å^2$. The size of the equilibrated
945 system was 360.000 × 480.809 × 260.784 $Å^3$. Then, the constraint was turned off
946 and only the box size along the x direction was allowed to move to observe the
947 fluctuation of half helical pitch (HHP), rise, and axial distance (AD) between
948 adjacent protomers along the same long-pitch strand. 100 ns MD simulation was
949 similarly performed for flexible and frozen alpha-actinin in the unipolar crosslinking
950 model, and the trajectories saved at 100 ps were used for the analyses. In the

951 same way, the system was built and the simulation was performed for the bipolar
952 configuration, but the number of water molecules was 1,432,853. To build a bare
953 actin fiber system, the alpha-actinin was removed from the unipolar system, and
954 100 ps MD simulation with constant temperature (300 K) and pressure conditions
955 (1 bar) was performed to fill the space originally located by the alpha-actinin. MD
956 simulations were similarly performed for 100 ns.

957 ***Principal component analysis***

958 Before the PCA, the configuration of alpha-actinin was aligned assuming
959 that C_α atoms in the center part of the rod domain (residue 485-525) have the
960 lowest root mean square fluctuation (RMSF).

961 To compare the conformational library of AFMfit and MD simulations for
962 Ca^{2+}-bound and Ca^{2+}-unbound states, we chose to reduce the dimensionality of
963 the libraries using PCA. We normalized the number of elements in the four
964 conformational libraries of AFMfit and MD simulations for Ca^{2+}-bound and Ca^{2+}-
965 unbound states, ensuring each library contains 1,000 conformations. We
966 combined these libraries to obtain a total library of 4,000 conformations. These
967 conformations were then projected onto the same subspace using PCA. Then PCA
968 was performed using singular value decomposition (SVD)[106] on the mean-
969 subtracted C_α coordinates of the combined libraries. We reduced the dimension to
970 three principal components by retaining only the principal components (PCs) that
971 have the most impact on the variance, more precisely the PCs that have an
972 explained variance ratio (i.e. the normalized squared singular values) of more than
973 10%. To obtain a subspace on a per-atom basis, the eigenvectors were normalized
974 by the number of C_α atoms in the system.

975 After performing MD simulations, we also conducted the analyses of alpha-
976 actinin conformations obtained from both unipolar and bipolar models using PCA.
977 This approach allowed us to capture their atomic conformational dynamics,
978 enabling an evaluation of the physical motion effects such as bending, twisting,
979 and rotation of alpha-actinin on fluctuations of the rise or AD in the crosslinked
980 actin filaments.

981 ***Analyses of domain distances and twisting and bending angles in alpha-***
982 ***actinin***

983 The ABD was divided into two domains: CH1, residue 26-138; CH2, residue
984 139-251. EF12 is residue 749-818, and EF34 is residue 819-888. The center of C_α
985 of each domain was used to compute domain distances. Since there are four
986 centers, there are six distances.

987 For the analyses of bending and twisting angles, the alpha-actinin was
988 aligned as described in PCA. The C_α atoms in residue 485-525 were placed on the
989 xy-plane and their average coordinate was set to be the origin. The rod domain
990 was placed along the x-axis (**Supplementary Fig. 4A**). The position of the center
991 of C_α atoms of CH1 and CH2 in one chain and EF12 and EF34 in the other chain
992 is denoted as (x_1, y_1, z_1) (end 1), and that of the other end (end 2) is denoted as
993 (x_2, y_2, z_2). x_1 is chosen so that $x_1 > 0$, so $x_2 < 0$. The bending angle for end 1 was
994 calculated by $\tan^{-1}(z_1/x_1)$, and that for end 2 by $-\tan^{-1}(z_2/x_2)$. In this definition, the
995 bending angles in alpha-actinin (PDB ID: 1SJJ) were −1.4 and 8.5 degrees.

996 For the twisting angle calculation, the position of the center of Cα atoms of
997 CH1 and CH2 at end 1 is denoted as (x_{1c}, y_{1c}, z_{1c}), and that of EF12 and EF34 at
998 end 1 is denoted as (x_{1e}, y_{1e}, z_{1e}). The twisting angle for end 1 was defined as the
999 angle between a vector from the center of EF12 and EF34 to the center of CH1
1000 and CH2 in the yz-plane and y axis (**Supplementary Fig. 4B**): that is, $\tan^{-1}((z_{1c} -$
1001 $z_{1e})/(y_{1c} - y_{1e}))$. For end 2, considering the orientation, it was calculated by
1002 $\tan^{-1}(-(z_{2c} - z_{2e})/(y_{2c} - y_{2e}))$. When the twisting angle became less than −100
1003 degrees, 360 degrees was added to the angle, since it is a part of the fluctuation
1004 over 180 degrees. In this definition, the twisting angles in alpha-actinin (PDB ID:
1005 1SJJ) were −12.8 and 20.5 degrees.

1006 ***Analyses of half helical pitch, rise and axial distance***

1007 We analyzed HHP, rise, and AD in bare actin filaments and in actin
1008 filaments crosslinked with flexible and frozen alpha-actinin, comprising both bipolar
1009 and unipolar crosslinking models obtained by MD simulations. In the MD
1010 simulations of actin filaments, the box along the filaments was allowed to move.

The HHP corresponds to the box length along this direction. The rise was defined as the average distance between the centers of mass of two adjacent protomers along the double-strand filament axis. Whereas, the AD was determined as the average distance between the centers of mass between adjacent protomers along the same long-pitch strand or the same protofilament axis (**Fig. 5A, C**).

Methods for measuring alpha-actinin crosslinking angles and inter-filament spacing

Alpha-actinin molecules crosslink two actin filaments in either a parallel (unipolar) or anti-parallel (bipolar) configuration. In this study, we analyzed the crosslinking angles (both small and large) relative to the filament axis and inter-filament spacing between actin filaments based on unipolar crosslinking conformations obtained from HS-AFM (**Supplementary Fig. 10**) and based on unipolar and bipolar configurations from MD simulations (**Fig. 5A, B**). Two alpha-actinin molecules consistently intercalated between actin filaments at every half-helical turn, forming a parallelogram-like configuration.

To analyze the conformations derived from HS-AFM, we tracked the center of mass (CoM) positions of four crossover points (e.g., A, B, C, and D in **Supplementary Fig. 10**) in a parallelogram, using their vertex coordinates. This process was performed with the Kodec software to semi-automatically detect the CoM positions (including its source code)[22].

To compute the interior angles of a parallelogram when the vertex coordinates were known, we followed these steps:

Given four vertices—A (x1, y1), B (x2, y2), C (x3, y3), and D (x4, y4)—arranged sequentially around the parallelogram, the first step was to determine the four vectors representing its sides:

$$\overrightarrow{AB} = (x2 - x1), (y2 - y1)$$

$$\overrightarrow{AD} = (x4 - x1), (y4 - y1)$$

$$\overrightarrow{BC} = (x3 - x2), (y3 - y2)$$

$$\overrightarrow{CD} = (x4 - x3), (y4 - y3)$$

Second, the angle between two vectors were calculated as:

Angle at A: between $\overrightarrow{AD}$ and $\overrightarrow{AB}$

Angle at B: between $\overrightarrow{AB}$ and $\overrightarrow{BC}$

Angle at C: between $\overrightarrow{BC}$ and $\overrightarrow{CD}$

Angle at D: between $\overrightarrow{CD}$ and $\overrightarrow{AD}$

For example, an angle θ (rad) at A:

$$\theta = \arccos \frac{(\mathrm{x}2 - x1)(x4 - x1) + (y2 - y1)(y4 - y1)}{\sqrt{(x2 - x1)^2 + (y2 - y1)^2}.\sqrt{(x4 - x1)^2 + (y4 - y1)^2}}$$

The angle (degrees) at A was then calculated:

$$\theta\ (deg) = \theta\ (rad) \frac{180}{\pi}$$

The angles at B, C, and D were calculated using the same approach. Finally, the physical lengths of AB, BC, CD, and DA segments were similarly determined and converted the lengths from pixel to nm unit.

Length of AB segment: $L\ (nm) = \frac{\mathrm{nm*pixel}}{\mathrm{pixel}} \sqrt{(x2 - x1)^2 + (y2 - y1)^2}$

The similar approach was utilized to analyze the unipolar and bipolar crosslinking conformations obtained from MD simulations. We noted that the definition of inter-filament measurements in HS-AFM and MD simulation data differed slightly, as described in their respective captions (**Supplementary Fig. 10**).

Data availability

All the data are included in the Supplementary Information or as source data. The conformation libraries, available in PDB format, can be accessed upon reasonable request and are open for AI-based training collaboration.

Code availability

https://gricad-gitlab.univ-grenoble-alpes.fr/GruLab/afmfit

Acknowledgments

The authors express their gratitude for the facility and financial support provided by the WPI Nano Life Science Institute (WPI NanoLSI), Kanazawa University; the instrumental assistance provided by Toshio Ando, Noriyuki Kodera, and Hiroki Konno (WPI NanoLSI); and the initial bipolar and unipolar models presented by Kenneth A. Taylor (Florida State University); and initial AFM data analysis by Thao Phuong Ngo and Thien Quang Huynh (WPI-NanoLSI). The authors also acknowledge the financial support from KAKENHI (Japan Society for the Promotion of Science) for K.X.N. (19K06581, 23K05713, 23H02452-01), T.S. (24K01308), and T.Q.P.U. (23H02452). The MD simulations were carried out on the supercomputers at the Research Center for Computational Science in Okazaki, Japan (Project: 24-IMS-096).

This study was also partially supported by the French National Research Agency (research grant ANR-23-CE45-0024-01) and within the framework of the "Investissements d'avenir" program (ANR-15-IDEX-02) for S.G.

1078 **Author Contributions:**

1079 K.X.N. designed the research; K.X.N., T.S., R.V. and S.G. performed the research;
1080 K.X.N., T.S., R.V., H.G.N., T.Q.P.U., N.T.P.L., and S.G. analyzed the data; K.X.N.,
1081 T.S., R.V. and S.G. wrote the paper.

1082 **Declaration of interests:**

1083 The authors declare that they have no competing interests.

1084 **Declaration of generative AI and AI-assisted technology**

1085 During the preparation of this work, the authors used ChatGPT to enhance the
1086 clarity of the English in their writing. After utilizing this tool, they carefully reviewed
1087 and edited the content as necessary and take full responsibility for the final
1088 publication. Furthermore, the manuscript has been submitted for scientific and
1089 English editing through Nature Springer's service.

1090

1091 **References**

1092 1. Fukami, K. *et al.* Requirement of phosphatidylinositol 4,5-bisphosphate for
1093 α-actinin function. *Nature* **359**, 150–152 (1992).

1094 2. Fraley, T. S. *et al.* Phosphoinositide binding inhibits α-actinin bundling
1095 activity. *J. Biol. Chem.* **278**, 24039–24045 (2003).

1096 3. Taylor, K. a & Taylor, D. W. Formation of two-dimensional complexes of F-
1097 actin and crosslinking proteins on lipid monolayers: demonstration of
1098 unipolar alpha-actinin-F-actin crosslinking. *Biophys. J.* **67**, 1976–83 (1994).

1099 4. Young, P. The interaction of titin and alpha-actinin is controlled by a
1100 phospholipid-regulated intramolecular pseudoligand mechanism. *EMBO J.*
1101 **19**, 6331–6340 (2000).

1102 5. Ribeiro, E. D. A. *et al.* The structure and regulation of human muscle α-
1103 Actinin. *Cell* **159**, 1447–1460 (2014).

1104 6. Liu, J., Taylor, D. W. & Taylor, K. A. A 3-D reconstruction of smooth muscle
1105 α-actinin by CryoEm reveals two different conformations at the actin-

1106 binding region. *J. Mol. Biol.* **338**, 115–125 (2004).

1107 7. Foley, K. S. & Young, P. W. The non-muscle functions of actinins: An
1108 update. *Biochem. J.* **459**, 1–13 (2014).

1109 8. Pinotsis, N. *et al.* Calcium modulates the domain flexibility and function of
1110 an α-actinin similar to the ancestral a-actinin. *Proc. Natl. Acad. Sci. U. S. A.*
1111 **117**, 22101–22112 (2020).

1112 9. Tang, J., Taylor, D. W. & Taylor, K. a. The three-dimensional structure of
1113 alpha-actinin obtained by cryoelectron microscopy suggests a model for
1114 Ca(2+)-dependent actin binding. *J. Mol. Biol.* **310**, 845–58 (2001).

1115 10. Pollard, T. D. & Cooper, J. A. Actin, a central player in cell shape and
1116 movement. *Science* **326**, 1208–1212 (2009).

1117 11. Fernandez, M. K., Sinha, M., Zidan, M. & Renz, M. Nuclear actin
1118 filaments–a historical perspective. *Nucleus* **15**, (2024).

1119 12. Egelman, E. H. Actin Filament Structure: The ghost of ribbons past. *Curr.*
1120 *Biol.* **4**, 79–81 (1994).

1121 13. Fujii, T., Iwane, A. H., Yanagida, T. & Namba, K. Direct visualization of
1122 secondary structures of F-actin by electron cryomicroscopy. *Nature* **467**,
1123 724–728 (2010).

1124 14. Holmes, K. C., Popp, D., Gebhard, W. & Kabsch, W. Atomic model of the
1125 actin filament. *Nature* **347**, 44–49 (1990).

1126 15. Lorenz, M., Popp, D. & Holmes, K. C. Refinement of the F-actin model
1127 against x-ray fiber diffraction data by the use of a directed mutation
1128 algorithm. *J. Mol. Biol.* **234**, 826–836 (1993).

1129 16. Oda, T., Iwasa, M., Aihara, T., Maéda, Y. & Narita, A. The nature of the
1130 globular- to fibrous-actin transition. *Nature* **457**, 441–445 (2009).

1131 17. Uyeda, T. Q. P., Yamazaki, Y., Kijima, S. T., Noguchi, T. Q. P. & Ngo, K. X.
1132 Multiple Mechanisms to Regulate Actin Functions : “ Fundamental ” Versus
1133 Lineage-Specific Mechanisms and Hierarchical Relationships.
1134 *Biomolecules* **15**, 1–37 (2025).

1135 18. Tsuda, Y., Yasutake, H., Ishuima, A. & Yanaogida, T. Torsional rigidity of
1136 single actin filaments and actin-actin bond breaking force under torsion
1137 measured directly by in vitro micromanipulation. *Proc. Natl. Acad. Sci. U.*
1138 *S. A.* **93**, 12937–12942 (1996).

1139 19. ben-Avraham, D. & Tirion, M. M. Dynamic and elastic properties of F-actin:
1140 a normal-modes analysis. *Biophys. J.* **68**, 1231–1245 (1995).

1141 20. Okura, K., Matsumoto, T., Narita, A. & Tatsumi, H. Mechanical Stress
1142 Decreases the Amplitude of Twisting and Bending Fluctuations of Actin
1143 Filaments. *J. Mol. Biol.* **435**, 168295 (2023).

1144 21. Sun, Z. G. & Murrell, M. Cofilin-Mediated Filament Softening and
1145 Crosslinking Counterbalance to Enhance Actin Network Flexibility. *Phys.*
1146 *Rev. Lett.* **133**, 218402 (2024).

1147 22. Ngo, K. X., Kodera, N., Katayama, E., Ando, T. & Uyeda, T. Q. Cofilin-
1148 induced unidirectional cooperative conformational changes in actin
1149 filaments revealed by high-speed atomic force microscopy. *Elife* **4**, 1–22
1150 (2015).

1151 23. Ngo, K. X. *et al.* Allosteric regulation by cooperative conformational
1152 changes of actin filaments drives mutually exclusive binding with cofilin and
1153 myosin. *Sci. Rep.* **6**, 1–11 (2016).

1154 24. Ngo, K. X. *et al.* Deciphering the actin structure dependent preferential
1155 cooperative binding of cofilin. *Elife* **13**, 1–37 (2024).

1156 25. Fineberg, A. *et al.* Myosin-5 varies its step length to carry cargo straight

1157 along the irregular F-actin track. *Proc. Natl. Acad. Sci.* **121**, 1–12 (2024).

1158 26. Ngo, K. X. *et al.* Allosteric regulation by cooperative conformational
1159 changes of actin filaments drives mutually exclusive binding with cofilin and
1160 myosin. *Sci. Rep.* **6**, 1–11 (2016).

1161 27. Hayakawa, Y. *et al.* Actin binding domain of Rng2 sparsely bound on F-
1162 actin strongly inhibits actin movement on myosin II. *Life Sci. Alliance* **6**,
1163 e202201469 (2022).

1164 28. Uyeda, T. Q. P., Iwadate, Y., Umeki, N., Nagasaki, A. & Yumura, S.
1165 Stretching actin filaments within cells enhances their affinity for the myosin
1166 ii motor domain. *PLoS One* **6**, e26200 (2011).

1167 29. Sharma, S., Grintsevich, E. E., Phillips, M. L., Reisler, E. & Gimzewski, J.
1168 K. Atomic Force Microscopy Reveals Drebrin Induced Remodeling of. 825–
1169 827 (2011).

1170 30. Hanein, D., Matsudaira, P. & DeRosier, D. J. Evidence of a conformational
1171 change in actin induced by fimbrin (N375) binding. *J. Cell Biol.* **139**, 387–
1172 396 (1997).

1173 31. Hosokawa, N. *et al.* Unidirectional cooperative binding of fimbrin actin-
1174 binding domain 2 to actin filament. *Biochem. Biophys. Res. Commun.* **552**,
1175 59–65 (2021).

1176 32. Ando, T. *et al.* A high-speed atomic force microscope for studying
1177 biological macromolecules. *Proc. Natl. Acad. Sci. U. S. A.* **98**, 12468–
1178 12472 (2001).

1179 33. Ando, T. *et al.* High-speed AFM and nano-visualization of biomolecular
1180 processes. *Pflugers Arch. Eur. J. Physiol.* **456**, 211–225 (2008).

1181 34. Ando, T., Fukuda, S., Ngo, K. X. & Flechsig, H. High-Speed Atomic Force
1182 Microscopy for Filming Protein Molecules in Dynamic Action. *Annu. Rev.*

1183 *Biophys.* **53**, 19–40 (2024).

1184 35. Homma, H. *et al.* PQBP3/NOL7 is an intrinsically disordered protein.
1185 *Biochem. Biophys. Res. Commun.* **736**, 150453 (2024).

1186 36. Kodera, N. *et al.* Structural and dynamics analysis of intrinsically
1187 disordered proteins by high-speed atomic force microscopy. *Nat.*
1188 *Nanotechnol.* **16**, 181–189 (2021).

1189 37. Fukuda, S. & Ando, T. Faster high-speed atomic force microscopy for
1190 imaging of biomolecular processes. *Rev. Sci. Instrum.* **92**, (2021).

1191 38. Shimizu, M. *et al.* An ultrafast piezoelectric Z-scanner with a resonance
1192 frequency above 1.1 MHz for high-speed atomic force microscopy. *Rev.*
1193 *Sci. Instrum.* **93**, 013701 (2022).

1194 39. Zwier, M. C. & Chong, L. T. Reaching biological timescales with all-atom
1195 molecular dynamics simulations. *Curr. Opin. Pharmacol.* **10**, 745–752
1196 (2010).

1197 40. Hollingsworth, S. A. & Dror, R. O. Molecular dynamics simulation for all.
1198 *Neuron* **99**, 1–29 (2018).

1199 41. Karplus, M. & McCammon, J. A. Molecular dynamics simulations of
1200 biomolecules. *Nat. Struct. Biol.* **9**, 646–652 (2002).

1201 42. Kovermann, M., Rogne, P. & Wolf-Watz, M. Protein dynamics and function
1202 from solution state NMR spectroscopy. *Q. Rev. Biophys.* **49**, e6 (2016).

1203 43. Hu, Y. *et al.* NMR-Based Methods for Protein Analysis. *Anal. Chem.* **93**,
1204 1866–1879 (2021).

1205 44. Golji, J., Collins, R. & Mofrad, M. R. K. Molecular mechanics of the α-
1206 actinin rod domain: Bending, torsional, and extensional behavior. *PLoS*
1207 *Comput. Biol.* **5**, (2009).

1208 45. Adcock, S. A. & McCammon, J. A. Molecular dynamics: Survey of methods
1209 for simulating the activity of proteins. *Chem. Rev.* **106**, 1589–1615 (2006).

1210 46. Sumino, A., Sumikama, T., Uchihashi, T. & Oiki, S. High-speed AFM
1211 reveals accelerated binding of agitoxin-2 to a K+ channel by induced fit.
1212 *Sci. Adv.* **5**, 1–10 (2019).

1213 47. Chu, J. W. & Voth, G. A. Allostery of actin filaments: Molecular dynamics
1214 simulations and coarse-grained analysis. *Proc. Natl. Acad. Sci. U. S. A.*
1215 **102**, 13111–13116 (2005).

1216 48. Li, M. & Zheng, W. All-atom molecular dynamics simulations of actin-
1217 myosin interactions: A comparative study of cardiac α myosin, β myosin,
1218 and fast skeletal muscle myosin. *Biochemistry* **52**, 8393–8405 (2013).

1219 49. Yu, I. *et al.* Biomolecular interactions modulate macromolecular structure
1220 and dynamics in atomistic model of a bacterial cytoplasm. *Elife* **5**, 1–22
1221 (2016).

1222 50. Lindorff-Larsen, K., Piana, S., Dror, R. O. & Shaw, D. E. How fast-folding
1223 proteins fold. *Science (80-.).* **334**, 517–520 (2011).

1224 51. Vakser, I. A., Grudinin, S., Jenkins, N. W., Kundrotas, P. J. & Deeds, E. J.
1225 Docking-based long timescale simulation of cell-size protein systems at
1226 atomic resolution. *Proc. Natl. Acad. Sci. U. S. A.* **119**, 1–8 (2022).

1227 52. Feig, M. & Sugita, Y. Whole-cell models and simulations in molecular
1228 detail. *Annu. Rev. Cell Dev. Biol.* **35**, 191–211 (2019).

1229 53. Ando, T., Fukuda, S., Ngo, K. X. & Flechsig, H. High-Speed Atomic Force
1230 Microscopy for Filming Protein Molecules in Dynamic Action. *Annu. Rev.*
1231 *Biophys.* **53**, 19–39 (2024).

1232 54. Hoffmann, A. & Grudinin, S. NOLB: Nonlinear Rigid Block Normal-Mode
1233 Analysis Method. *J. Chem. Theory Comput.* **13**, 2123–2134 (2017).

1234 55. Tama, F. & Sanejouand, Y. H. Conformational change of proteins arising
1235 from normal mode calculations. *Protein Eng.* **14**, 1–6 (2001).

1236 56. Tama, F., Valle, M., Frankt, J. & Brooks, C. L. Dynamic reorganization of
1237 the functionally active ribosome explored by normal mode analysis and
1238 cryo-electron microscopy. *Proc. Natl. Acad. Sci. U. S. A.* **100**, 9319–9323
1239 (2003).

1240 57. Vuillemot, R., Pellequer, J. & Grudinin, S. AFMfit : Deciphering
1241 conformational dynamics in AFM data using fast nonlinear NMA and FFT-
1242 based search. *bioRxiv* (2024). doi:10.1101/2024.06.03.597083

1243 58. Shams, H., Golji, J., Garakani, K. & Mofrad, M. R. K. Dynamic Regulation
1244 of α-Actinin's Calponin Homology Domains on F-Actin. *Biophys. J.* **110**,
1245 1444–1455 (2016).

1246 59. Skwarek-Maruszewska, A., Hotulainen, P., Mattila, P. K. & Lappalainen, P.
1247 Contractility-dependent actin dynamics in cardiomyocyte sarcomeres. *J.*
1248 *Cell Sci.* **122**, 2119–2126 (2009).

1249 60. Martin, T. G. & Kirk, J. A. Under construction: The dynamic assembly,
1250 maintenance, and degradation of the cardiac sarcomere. *J. Mol. Cell.*
1251 *Cardiol.* **148**, 89–102 (2020).

1252 61. Tojkander, S., Gateva, G. & Lappalainen, P. Actin stress fibers - Assembly,
1253 dynamics and biological roles. *J. Cell Sci.* **125**, 1855–1864 (2012).

1254 62. Rajan, S., Kudryashov, D. S. & Reisler, E. Actin Bundles Dynamics and
1255 Architecture. *Biomolecules* **13**, (2023).

1256 63. Taylor, K. A., Taylor, D. W. & Schachat, F. Isoforms of α-actinin from
1257 cardiac, smooth, and skeletal muscle form polar arrays of actin filaments.
1258 *J. Cell Biol.* **149**, 635–645 (2000).

1259 64. Taylor, K. a & Taylor, D. W. Formation of 2-D paracrystals of F-actin on

1260 phospholipid layers mixed with quaternary ammonium surfactants. *J.*
1261 *Struct. Biol.* **108**, 140–7 (2008).

1262 65. Ando, T. High-speed atomic force microscopy coming of age.
1263 *Nanotechnology* **23**, 1–27 (2012).

1264 66. Ando, T., Uchihashi, T. & Fukuma, T. High-speed atomic force microscopy
1265 for nano-visualization of dynamic biomolecular processes. *Prog. Surf. Sci.*
1266 **83**, 337–437 (2008).

1267 67. David A. Begg, Richard Rodewald, L. I. R. The VISUALIZATION OF
1268 ACTIN FILAMENT POLARITY IN THIN SECTIONS Evidence for the
1269 Uniform Polarity of Membrane-Associated Filaments. *J. Cell Biol.* **79**, 846–
1270 852 (1978).

1271 68. Andrianantoandro, E. & Pollard, T. D. Mechanism of Actin Filament
1272 Turnover by Severing and Nucleation at Different Concentrations of
1273 ADF/Cofilin. *Mol. Cell* **24**, 13–23 (2006).

1274 69. Egelman, E. H., Francis, N. & DeRosier, D. J. F-actin is a helix with a
1275 random variable twist. *Nature* **298**, 131–135 (1982).

1276 70. McGough, A., Pope, B., Chiu, W. & Weeds, A. Cofilin changes the twist of
1277 F-actin: implications for actin filament dynamics and cellular function. *J.*
1278 *Cell Biol.* **138**, 771–781 (1997).

1279 71. Galkin, V. E. *et al.* Remodeling of actin filaments by ADF/cofilin proteins.
1280 *Proc. Natl. Acad. Sci. U. S. A.* **108**, 20568–20572 (2011).

1281 72. Tanaka, K. *et al.* Structural basis for cofilin binding and actin filament
1282 disassembly. *Nat. Commun.* **9**, 1–3 (2018).

1283 73. Reynolds, M. J., Hachicho, C., Carl, A. G., Gong, R. & Alushin, G. M.
1284 Bending forces and nucleotide state jointly regulate F-actin structure.
1285 *Nature* (2022). doi:10.1038/s41586-022-05366-w

1286 74. Voss, J. M., Harder, O. F., Olshin, P. K., Drabbels, M. & Lorenz, U. J.
1287 Rapid melting and revitrification as an approach to microsecond time-
1288 resolved cryo-electron microscopy. *Chem. Phys. Lett.* **778**, 138812 (2021).

1289 75. Bongiovanni, G., Harder, O. F., Drabbels, M. & Lorenz, U. J. Microsecond
1290 melting and revitrification of cryo samples with a correlative light-electron
1291 microscopy approach. *Front. Mol. Biosci.* **9**, 1–7 (2022).

1292 76. Lorenz, U. J. Microsecond time-resolved cryo-electron microscopy. *Curr.*
1293 *Opin. Struct. Biol.* **87**, 102840 (2024).

1294 77. Vuillemot, R., Miyashita, O., Tama, F., Rouiller, I. & Jonic, S. NMMD:
1295 Efficient Cryo-EM Flexible Fitting Based on Simultaneous Normal Mode
1296 and Molecular Dynamics atomic displacements. *J. Mol. Biol.* **434**, 167483
1297 (2022).

1298 78. Boehr, D. D., Dyson, H. J. & Wright, P. E. An NMR perspective on enzyme
1299 dynamics. *Chem. Rev.* **106**, 3055–3079 (2006).

1300 79. Wolf-Watz, M. *et al.* Linkage between dynamics and catalysis in a
1301 thermophilic-mesophilic enzyme pair. *Nat. Struct. Mol. Biol.* **11**, 945–949
1302 (2004).

1303 80. Purslow, J. A., Khatiwada, B., Bayro, M. J. & Venditti, V. NMR Methods for
1304 Structural Characterization of Protein-Protein Complexes. *Front. Mol.*
1305 *Biosci.* **7**, 1–8 (2020).

1306 81. Camacho-Zarco, A. R. *et al.* NMR Provides Unique Insight into the
1307 Functional Dynamics and Interactions of Intrinsically Disordered Proteins.
1308 *Chem. Rev.* **122**, 9331–9356 (2022).

1309 82. Moraes, A. H. & Valente, A. P. Conformational dynamics and kinetics of
1310 protein interactions by nuclear magnetic resonance. *J. Magn. Reson. Open*
1311 **14**–**15**, 100093 (2023).

1312 83. Murata, K. & Wolf, M. Cryo-electron microscopy for structural analysis of
1313 dynamic biological macromolecules. *Biochim. Biophys. Acta - Gen. Subj.*
1314 **1862**, 324–334 (2018).

1315 84. Gauto, D. F. *et al.* Integrated NMR and cryo-EM atomic-resolution structure
1316 determination of a half-megadalton enzyme complex. *Nat. Commun.* **10**, 1–
1317 12 (2019).

1318 85. Schanda, P. & Haran, G. NMR and Single-Molecule FRET Insights into
1319 Fast Protein Motions and Their Relation to Function. *Annu. Rev. Biophys.*
1320 **53**, 247–273 (2024).

1321 86. Murakami, K. *et al.* Structural basis for actin assembly, activation of ATP
1322 hydrolysis, and delayed phosphate release. *Cell* **143**, 275–287 (2010).

1323 87. González, M. A. Force fields and molecular dynamics simulations. *Collect.*
1324 *SFN* **12**, 169–200 (2011).

1325 88. Chmiela, S., Sauceda, H. E., Müller, K. R. & Tkatchenko, A. Towards exact
1326 molecular dynamics simulations with machine-learned force fields. *Nat.*
1327 *Commun.* **9**, 1–10 (2018).

1328 89. Bhavna, R. & Sonawane, M. A deep learning framework for quantitative
1329 analysis of actin microridges. *npj Syst. Biol. Appl.* **9**, 1–15 (2023).

1330 90. Degenhardt, M. F. S. *et al.* Determining structures of RNA conformers
1331 using AFM and deep neural networks. *Nature* **637**, (2025).

1332 91. Vinh, T., Nguyen, T., Ly, N. Q., Thi, N. & Le, P. Developing the
1333 Computational Image Processing Method for Quantitative Analysis of
1334 Nanopore Structure Obtained from HS-AFM (AFMnanoQ). *bioRxiv*
1335 (2025). doi:10.1101/2025.02.26.640237

1336 92. Jiang, Y., Wang, Z. & Scheuring, S. A structural biology compatible file
1337 format for atomic force microscopy. *Nat. Commun.* **16**, 1–16 (2025).

93. Sumikama, T. *et al.* Computed Three-Dimensional Atomic Force Microscopy Images of Biopolymers Using the Jarzynski Equality. *J. Phys. Chem. Lett.* **13**, 5365–5371 (2022).

94. Tetsuya Asakawa, N. A. Preparation of Subfragment-1 from Abalone Smooth Muscle Myosin. *J. Biochem.* **103**, 667–671 (1988).

95. Ando, T., Uchihashi, T. & Kodera, N. High-speed AFM and applications to biomolecular systems. *Annu. Rev. Biophys.* **42**, 393–414 (2013).

96. Tian, C. *et al.* Ff19SB: Amino-Acid-Specific Protein Backbone Parameters Trained against Quantum Mechanics Energy Surfaces in Solution. *J. Chem. Theory Comput.* **16**, 528–552 (2020).

97. William L. Jorgensen, Jayaraman Chandrasekhar, and J. D. M. Comparison of simple potential functions for simulating liquid water. *J. Chem. Phys.* **79**, 926–935 (1983).

98. Li, P., Song, L. F. & Merz, K. M. Systematic parameterization of monovalent ions employing the nonbonded model. *J. Chem. Theory Comput.* **11**, 1645–1657 (2015).

99. Li, P. & Merz, K. M. Taking into account the ion-induced dipole interaction in the nonbonded model of ions. *J. Chem. Theory Comput.* **10**, 289–297 (2014).

100. Berendsen, H. J. C., Postma, J. P. M., Van Gunsteren, W. F., Dinola, A. & Haak, J. R. Molecular dynamics with coupling to an external bath. *J. Chem. Phys.* **81**, 3684–3690 (1984).

101. Ryckaert, J. P., Ciccotti, G. & Berendsen, H. J. C. Numerical integration of the cartesian equations of motion of a system with constraints: molecular dynamics of n-alkanes. *J. Comput. Phys.* **23**, 327–341 (1977).

102. Essmann, U. *et al.* A smooth particle mesh Ewald method. *J. Chem. Phys.*

1364 **103**, 8577–8593 (1995).

1365 103. Kanematsu, Y. *et al.* Structures and mechanisms of actin ATP hydrolysis.
1366 *Proc. Natl. Acad. Sci. U. S. A.* **119**, 1–12 (2022).

1367 104. Meagher, K. L., Redman, L. T. & Carlson, H. A. Development of
1368 polyphosphate parameters for use with the AMBER force field. *J. Comput.*
1369 *Chem.* **24**, 1016–1025 (2003).

1370 105. Andrej Sali, T. L. B. Comparative Protein Modelling by Satisfaction of
1371 Spatial Restraints. *J. Mol. Biol.* **234**, 779–815 (1993).

1372 106. Wall, M. E., Rechtsteiner, A. & Rocha, L. M. Singular Value Decomposition
1373 and Principal Component Analysis. in *A Practical Approach to Microarray*
1374 *Data Analysis* 91–109 (2005). doi:10.1007/0-306-47815-3_5

1375 107. Amyot, R. & Flechsig, H. BioAFMviewer: An interactive interface for
1376 simulated AFM scanning of biomolecular structures and dynamics. *PLoS*
1377 *Comput. Biol.* **16**, 1–12 (2020).

1378 108. Hampton, C. M., Taylor, D. W. & Taylor, K. A. Novel structures for α-
1379 actinin: F-actin interactions and their implications for actin-membrane
1380 attachment and tension sensing in the cytoskeleton. *J. Mol. Biol.* **368**, 92–
1381 104 (2007).

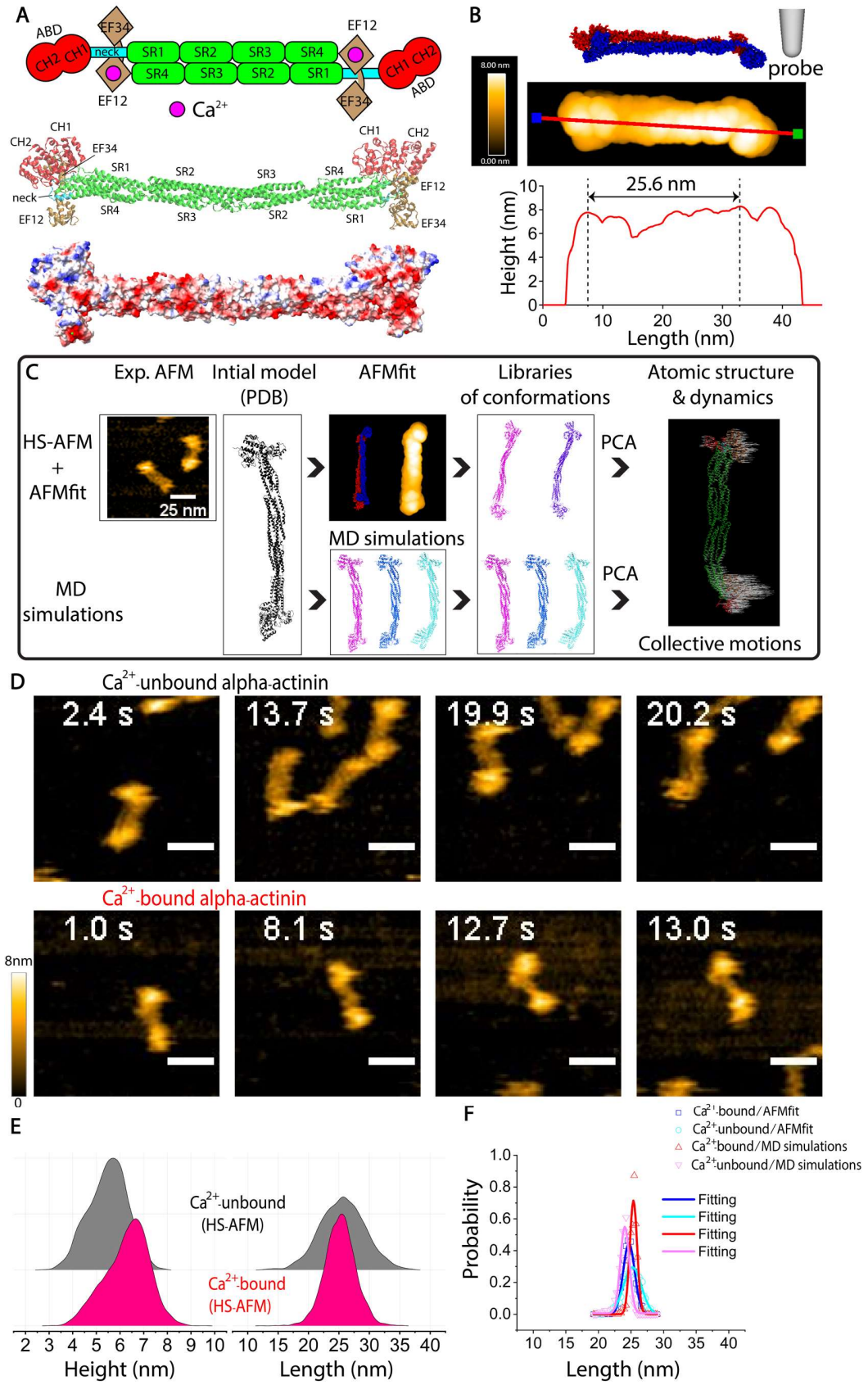
A
ABD
CH2 CH1
neck
EF34
EF12
SR1
SR2
SR3
SR4
Ca2+
B
probe
8.00 nm
0.00 nm
25.6 nm
Height (nm)
Length (nm)
C
Exp. AFM
Intial model (PDB)
AFMfit
Libraries of conformations
Atomic structure & dynamics
HS-AFM + AFMfit
25 nm
MD simulations
PCA
Collective motions
D
Ca2+-unbound alpha-actinin
2.4 s
13.7 s
19.9 s
20.2 s
Ca2+-bound alpha-actinin
1.0 s
8.1 s
12.7 s
13.0 s
8nm
0
E
Ca2+-unbound (HS-AFM)
Ca2+-bound (HS-AFM)
Height (nm)
Length (nm)
F
Ca2+-bound/AFMfit
Ca2+-unbound/AFMfit
Ca2+-bound/MD simulations
Ca2+-unbound/MD simulations
Fitting
Probability
Length (nm)

1382

1383 **Fig. 1 Novel workflow for analyzing the dynamics and atomic structures of**
1384 **alpha-actinin through the integration of HS-AFM with the AFMfit and MD**
1385 **simulations.**
1386 (**A**) Domain composition and structure of chicken gizzard smooth muscle alpha-
1387 actinin (PDB: 1SJJ) depicted in a ribbon model and an electrostatic surface
1388 potential model. In the latter, red and blue represent negative and positive charges,
1389 respectively. Alpha-actinin is an antiparallel homodimer with a molecular weight
1390 exceeding 200 kDa. It comprises an N-terminal actin binding domain (ABD), in
1391 which the two calponin homology 1 and 2 (CH1, CH2) domains are in extensive
1392 contact, a central region containing four spectrin-like repeat (SR1-SR4) or rod
1393 domains, and a C-terminal calmodulin-like domain (CaMD) that includes two pairs
1394 of EF-hand motifs (EF12 and EF34). The EF12 domain is responsible for the Ca^{2+}
1395 binding. The two ABDs undergo a 90-degree rotation, enabling alpha-actinin to
1396 crosslink the actin filaments in nearly any orientation.
1397 (**B**) Pseudo-AFM images and topographic cross-sectional profile of alpha-actinin
1398 generated with the AFM viewer[107]. The pseudo-AFM images were obtained with
1399 the following scan parameters: step size, 0.1 nm; cone angle, 5°; and tip radius,
1400 2.0 nm. The cross-sectional profile in the bottom panel corresponds to the red line
1401 in the middle panel.
1402 (**C**) Workflow for developing libraries of conformations, storing them as PDB files,
1403 and analyzing the dynamics and atomic structures of alpha-actinin through the
1404 integration of HS-AFM with the AFMfit and molecular dynamics (MD) simulations.
1405 This process is followed by principal component analysis (PCA) to identify and
1406 classify dynamic atomic structures into distinct modes of collective motion
1407 (indicated by white arrows).
1408 (**D**) HS-AFM still images showing the various physical motions of alpha-actinin,
1409 such as twisting and bending, with and without Ca^{2+} binding. Scale bars: 25 nm.
1410 Color scale: 0–8 nm.

(**E**) Ridgeline plots displaying the distribution of the peak heights and lengths between the two ABDs for Ca^{2+}-bound and Ca^{2+}-unbound alpha-actinin obtained with HS-AFM. A two-sample *t test* ($p \leq 0.05$) indicates that the differences in the distributions of the height and length between the bound and unbound states are significant ($p = 0$ for height, $p = 7.45454 \times 10^{-7}$ for length).

(**F**) Plot showing the length distributions between the two centers of mass of the CH1-CH2 and EF12-EF34 domains located on the opposite sides of alpha-actinin using data from the atomic conformations obtained from the AFMfit and MD simulations for both the Ca^{2+}-bound and Ca^{2+}-unbound states. The mean ± SD lengths were determined through single Gaussian fitting. A two-sample *t test* ($p \leq 0.05$) confirmed that the differences in the distributions of the length between the Ca^{2+}-bound and Ca^{2+}-unbound states were statistically significant ($p = 8.9 \times 10^{-28}$ for the AFMfit data; $p = 0$ for the MD simulations).

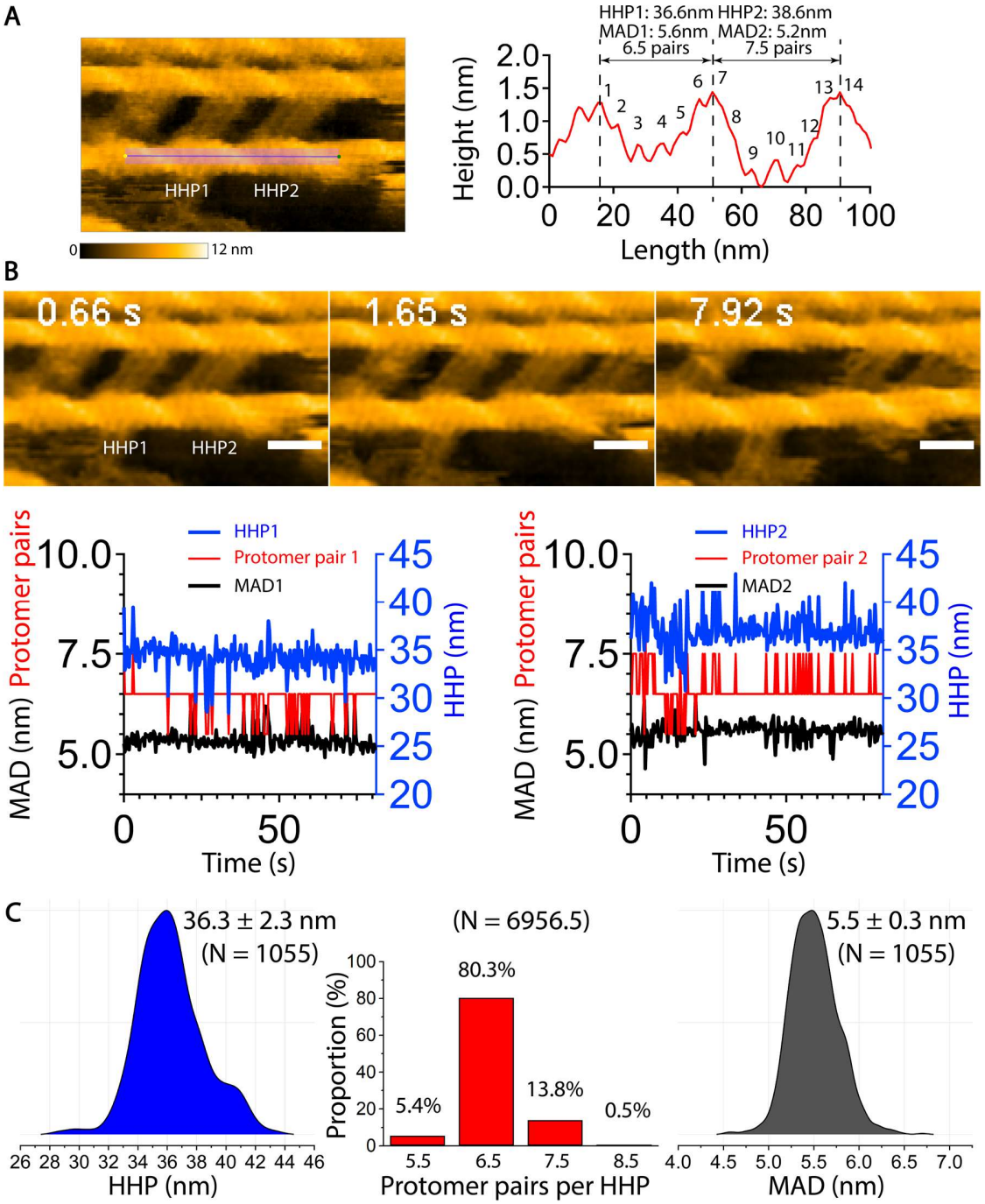

Fig. 2 HS-AFM-based analysis of the dynamic conformation of the actin filaments crosslinked with alpha-actinin in a unipolar configuration in the presence of ATP, Ca^{2+}, and S1.

1445 (**A**) Longitudinal section profile illustrating the analysis of the magnitudes of the
1446 two adjacent HHPs, the number of protomer pairs per HHP, and the MADs in
1447 various actin filaments captured at different time points with still AFM images. The
1448 analytic methods employed were developed previously[24].
1449 **(B)** Time-dependent changes in the magnitudes of two adjacent HHPs, the number
1450 of protomer pairs per HHP, and the MADs in the actin filaments crosslinked with
1451 50 nM α-actinin in the presence of 1 mM ATP, 0.1 mM $CaCl_2$, and 1 μM S1 but
1452 without $MgCl_2$. Scale bars: 25 nm. Color scale: 0–12 nm.
1453 **(C)** Ridgeline and bar plots displaying the distribution of the magnitude of the
1454 HHPs, the number of the protomer pairs per HHP, and the MADs, as well as the
1455 corresponding number of events (N) (1055, 6956.5, and 1055, respectively).
1456
1457
1458
1459
1460
1461
1462
1463
1464
1465
1466
1467
1468
1469
1470
1471
1472
1473
1474

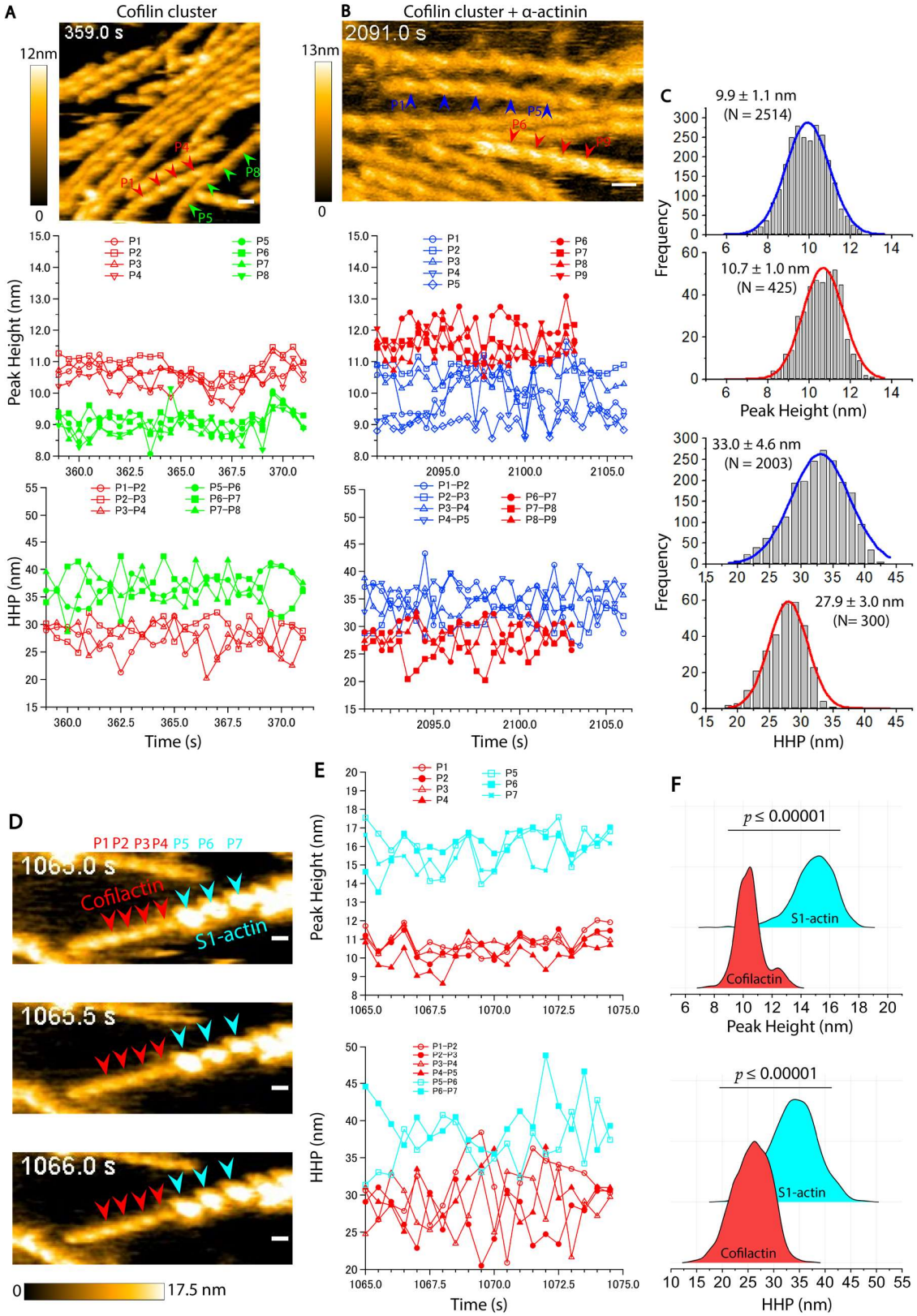
A
Cofilin cluster
359.0 s
12nm
0
P1
P2
P3
P4
P5
P6
P7
P8
Peak Height (nm)
HHP (nm)
Time (s)
B
Cofilin cluster + α-actinin
2091.0 s
13nm
0
P1
P2
P3
P4
P5
P6
P7
P8
P9
P1–P2
P2–P3
P3–P4
P4–P5
P5–P6
P6–P7
P7–P8
P8–P9
C
9.9 ± 1.1 nm
(N = 2514)
10.7 ± 1.0 nm
(N = 425)
33.0 ± 4.6 nm
(N = 2003)
27.9 ± 3.0 nm
(N= 300)
Frequency
Peak Height (nm)
HHP (nm)
D
P1 P2 P3 P4 P5 P6 P7
1065.0 s
Cofilactin
S1-actin
1065.5 s
1066.0 s
0
17.5 nm
E
Peak Height (nm)
HHP (nm)
Time (s)
F
p ≤ 0.00001
S1-actin
Cofilactin
Peak Height (nm)
p ≤ 0.00001
S1-actin
Cofilactin
HHP (nm)

1475

1476 **Fig. 3 The crosslinking of actin filaments by alpha-actinin inhibits both the**
1477 **development of mature cofilin clusters and shortening of HHP in actin**
1478 **filaments.**
1479 (**A**) Time-dependent changes in the peak heights and HHPs of actin filaments
1480 incubated with only 600 nM hs cofilin 1 and 1mM ATP. A ~25% decrease in HHP
1481 and the formation of mature cofilin clusters on actin filaments in the absence of
1482 alpha-actinin served as positive controls, providing a basis for comparison with the
1483 cofilin clusters and HHP shown in **B**. Red and green arrowheads indicate the peaks
1484 in mature cofilin clusters and bare actin segments (served as negative controls),
1485 respectively. Time label indicates the time after adding cofilin. Scale bars: 25 nm.
1486 Color scale: 0-12 nm. **Related to Supplementary Video 4A.**
1487 (**B**) Time-dependent changes in the peak heights and HHPs of actin filaments
1488 incubated 400 nM α-actinin and 1 mM ATP, and subsequently added with 600 nM
1489 cofilin. The cofilin binding and formation of mature cofilin clusters, and the
1490 shortening of HHP were significantly suppressed by crosslinking of alpha-actinin.
1491 Red arrowheads denote the peaks in mature cofilin clusters within the supertwisted
1492 half helices of actin segments (cofilactin) without alpha-actinin, and blue
1493 arrowheads indicate those in immature cofilin clusters within the long half helices
1494 of actin segments crosslinked with alpha-actinin (cofilactin-actinin), respectively.
1495 Scale bars: 25 nm. Color scale: 0-13 nm. **Related to Supplementary Video 4B.**

1496 (**C**) Histograms of the peak height and HHP measured from various actin filaments
1497 with and without alpha-actinin crosslinking, showing the presence of both mature
1498 and immature cofilin clusters. These clusters corresponded to short and long
1499 HHPs, respectively. Notably, their categorization as mature or immature clusters
1500 was based on their differences in peak heights and length of corresponding HHPs,
1501 and their comparisons with bare actin (i.e., peak height of 8.6 ± 0.8 nm, HHP of
1502 36.8 ± 4.3 nm), as reported in our previous studies[22]. The mean ± SD heights and
1503 lengths are 10.7 ± 1.0 nm (N = 425) and 27.9 ± 3.0 nm (N= 300) for mature clusters
1504 of cofilactin segment without alpha-actinin, and 9.9 ± 1.1 nm (N = 2514) and 33.0
1505 ± 4.6 nm (N = 2003) for immature clusters of cofilactin segment with alpha-actinin
1506 crosslinking (cofilactin-actinin). A two-population *t-test* ($p < 0.05$) indicates that the
1507 differences in height and HHP distribution between the clusters of cofilactin
1508 segments without and with alpha-actinin crosslinking are significant ($p = 2.9\text{x}10^{-38}$
1509 for height, $p = 8.5\text{x}10^{-68}$ for HHP).
1510 **(D)** Still AFM images show actin filaments with distinct short and long HHP regions
1511 where cofilin (cofilactin) and S1 (S1-actin) clusters bind. These filaments
1512 represented one of the configurations in **Supplementary Fig. 2B**. Red and cyan
1513 arrowheads mark cofilactin and S1-actin regions, respectively. Time labels
1514 correspond to frames in **Supplementary Video 6** after the addition of 100 nM
1515 cofilin, during which stable S1 clusters were formed near cofilin clusters on actin
1516 filaments when ATP levels were depleted. Scale bars: 25 nm. Color scale: 0-17.5
1517 nm.
1518 **(E)** Time-dependent variations in peak heights and HHP within cofilactin and S1-
1519 actin clusters.
1520 **(F)** Ridgeline plots displaying the distribution of peak heights and HHP in cofilactin
1521 and S1-actin cluster regions. The average peak heights (mean ± SD) are 10.5 ±
1522 1.0 nm (N = 935) for cofilactin and 14.9 ± 1.4 nm (N = 1051) for S1-actin segments.
1523 The average HHPs (mean ± SD) are 25.7 ± 3.6 nm (N = 767) for cofilactin and
1524 33.9 ± 4.4 nm (N = 805) for S1-actin. Statistical differences between mean values
1525 were analyzed using a two-population *t-test* and significant at ($p<0.00001$).

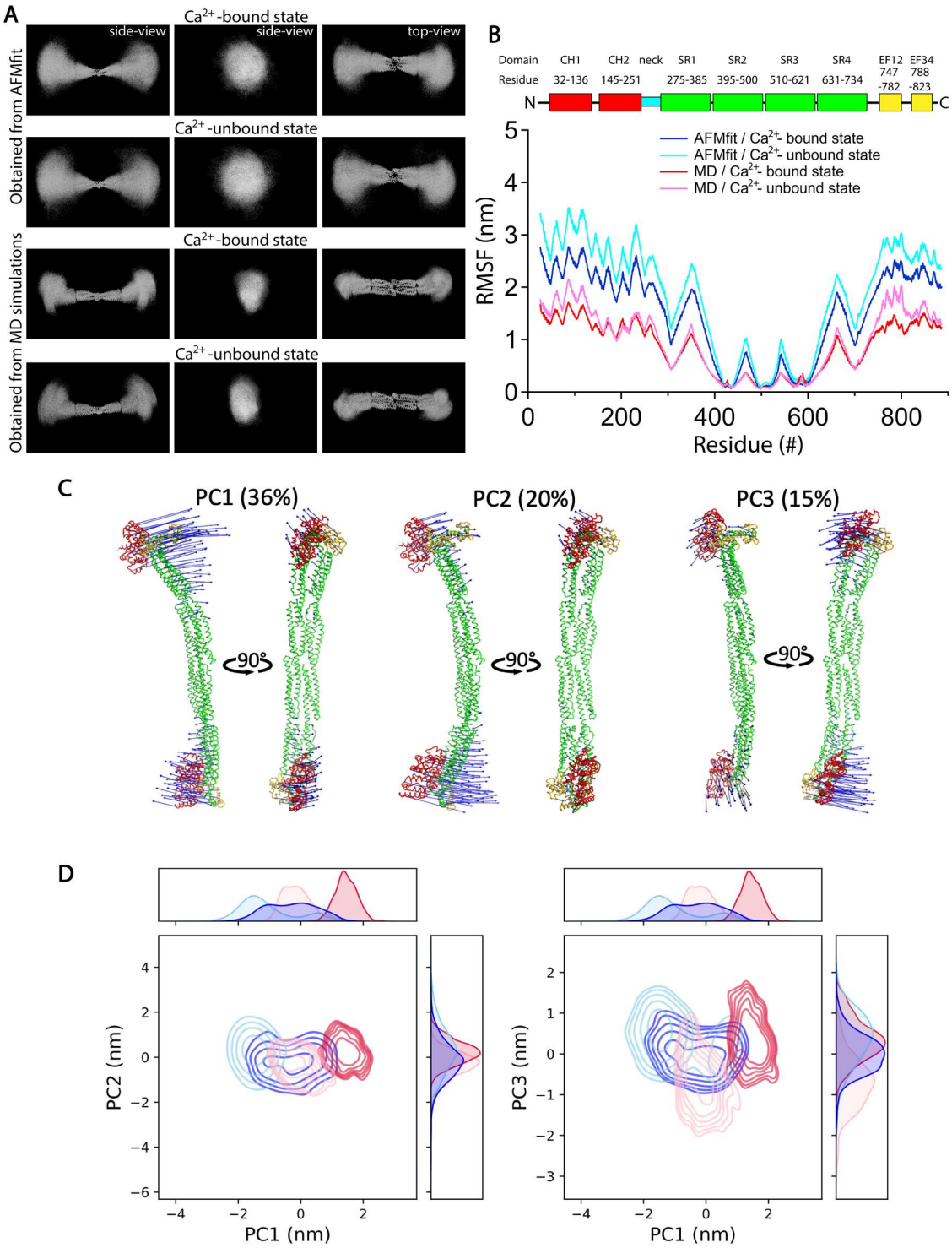
A
Ca2+-bound state
side-view
side-view
top-view
Ca2+-unbound state
Ca2+-bound state
Ca2+-unbound state
Obtained from AFMfit
Obtained from MD simulations
B
Domain
Residue
CH1
32-136
CH2
145-251
neck
SR1
275-385
SR2
395-500
SR3
510-621
SR4
631-734
EF12
747
-782
EF34
788
-823
N
C
AFMfit / Ca2+- bound state
AFMfit / Ca2+- unbound state
MD / Ca2+- bound state
MD / Ca2+- unbound state
RMSF (nm)
Residue (#)
C
PC1 (36%)
PC2 (20%)
PC3 (15%)
90°
90°
90°
D
PC2 (nm)
PC1 (nm)
PC3 (nm)
PC1 (nm)

1526

1527 **Fig. 4 Analyses of the dynamics and atomic structure of the Ca^{2+}-bound and**
1528 **unbound alpha-actinin using HS-AFM combined with the AFMfit and MD**
1529 **simulations.**
1530 (**A**) Positions of the Cα atoms from the libraries of the Ca^{2+}-bound and Ca^{2+}-
1531 unbound alpha-actinin conformations obtained from the AFMfit and MD
1532 simulations. The conformations were aligned, assuming that the helical elements
1533 in the SR2 and SR3 domains (residues 485-525) exhibited the lowest root mean
1534 square fluctuation (RMSF). Top views and two different side views are presented
1535 to compare the molecular dynamics among the states and conformation libraries.
1536 (**B**) RMSF values plotted against the residue number. The illustration of the alpha-
1537 actinin domains, along with their corresponding amino acid residues, is based on
1538 PDB ID 1SJJ, using colors consistent with those in **Fig. 1A**. From the N-terminus
1539 to the C-terminus: CH1, CH2: calponin homology 1 and 2; SR1-SR4: spectrin-like
1540 repeat 1-4; and EF12, EF34: EF hand motifs 12, 34.
1541 (**C**) Ensemble motions of the atomic conformations of alpha-actinin projected onto
1542 a common PCA space according to the conformational libraries of Ca^{2+}-bound and
1543 Ca^{2+}-unbound alpha-actinin obtained from the AFMfit and MD simulations. The
1544 eigenvalues of the principal components (PC1, PC2, PC3) were used to calculate
1545 the contributions (in percentages) of each motion to the total motions of alpha-
1546 actinin in the two states. The alpha-actinin structures are illustrated in the tube
1547 conformations, with the ABD, neck, rod, and EF12-EF34 domains represented in
1548 red, cyan, green, and yellow, respectively; the eigenvectors indicating the direction
1549 of motion are shown with blue arrows.
1550 (**D**) Distributions of PC1 and PC2 (left) and PC1 and PC3 (right). The values
1551 derived from the conformational libraries obtained from the AFMfit and MD
1552 simulations are plotted in blue and red, respectively. Light blue and light red
1553 represent the PCs obtained from the libraries corresponding to the Ca^{2+}-unbound
1554 state, whereas dark blue and dark red represent the PCs obtained from the
1555 libraries corresponding to the Ca^{2+}-bound state.
1556

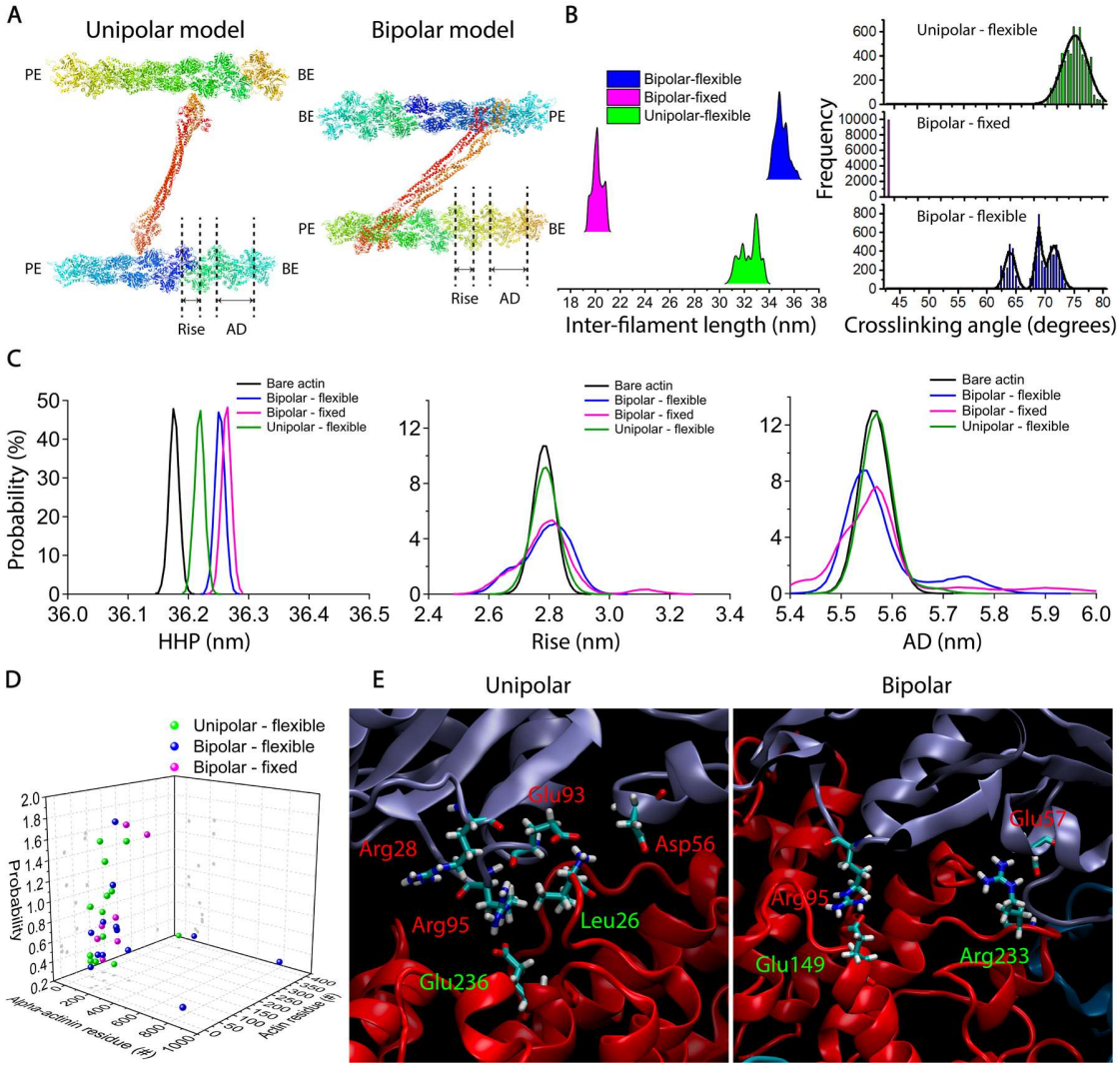

Fig. 5 Differences in the conformational changes in the actin filaments crosslinked with alpha-actinin in unipolar and bipolar models, including rise, AD, and residue-level interactions. (**A**) Illustrations of the unipolar and bipolar crosslinking models of the actin filaments with alpha-actinin. The unipolar crosslinking configuration occurs when the actin filaments share the same polarity, whereas the bipolar crosslinking configuration appears when the actin filaments align with opposite polarities. The rise and AD analyses were performed using conformations obtained from MD simulations. See the definitions of rise and AD in the Supplementary Methods.

(**B**) Quantitative analysis of the inter-filament lengths and alpha–actin crosslinking angles relative to the filament axis in the unipolar-flexible, bipolar-flexible, and bipolar-fixed models obtained from the MD simulations. In these models, the flexible condition allowed all Cα atoms in alpha-actinin to vibrate freely, while the fixed condition computationally constrained them.

(**C**) Analysis of the HHP, rise, and AD in the bare actin filaments and in the unipolar-flexible, bipolar-flexible, and bipolar-fixed models using the conformations derived from the MD simulations.

(**D, E**) Characterization of the residue-level interactions between the alpha-actinin ABDs and actin protomers during crosslinking in the unipolar-flexible and bipolar-flexible models. If an atom of one residue was in contact within 2 Å of an atom of another residue, these two residues were considered to be interacting. The probability of the residue contacts, time averaged contact probability, was calculated as the combined sum of interactions between the two alpha-actinin ABDs (green texts) and actin (red texts) residues, resulting in a maximum value of 2. Related to **Supplementary Table 1**.

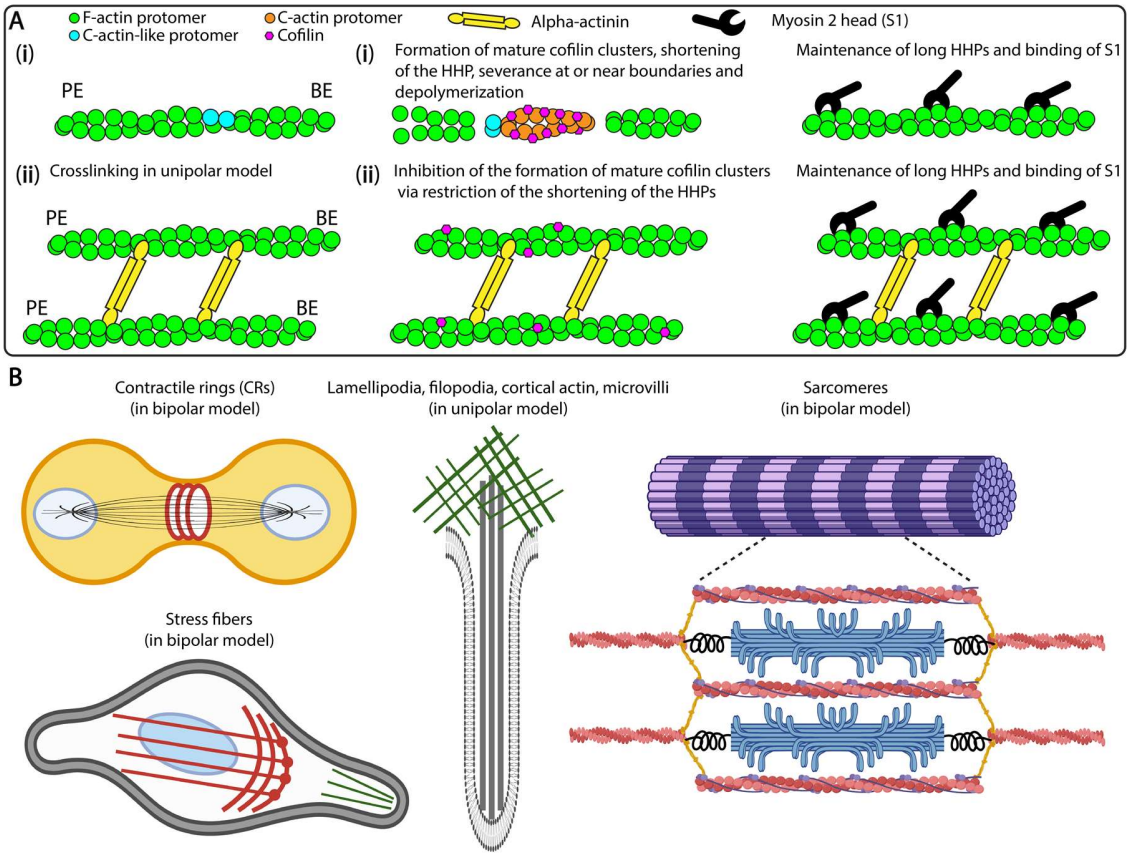

Fig. 6 Hypothesis outlining the configurations, functions, and localizations of the actin filaments and their crosslinking with alpha-actinin in both unipolar and bipolar models.

(**A**) Summary of our experimental findings on how the actin filaments and crosslinking of the unipolar actin filaments with alpha-actinin regulate the binding of S1 and cofilin.

(**B**) Illustration depicting the unipolar and bipolar crosslinking conformations, highlighting their distinct localizations and functions within cells. This figure was created using BioRender.com. Related to **Supplementary Table 2**.

Supplementary Information for

Atomic Conformational Dynamics and Actin-Crosslinking Function of Alpha-Actinin Revealed by SimHS-AFMfit

Kien Xuan Ngo, Takashi Sumikama, Rémi Vuillemot, Han Gia Nguyen, Taro QP Uyeda, Ngan Thi Phuong Le, Sergei Grudinin

Email:

ngoxuankien@staff.kanazawa-u.ac.jp

sumi@staff.kanazawa-u.ac.jp

remi.vuillemot@univ-grenoble-alpes.fr

sergei.grudinin@univ-grenoble-alpes.fr

This PDF file includes:

Supplementary Figures 1 to 10

Supplementary Tables 1 to 2

Supplementary Videos 1 to 20

Supplementary References

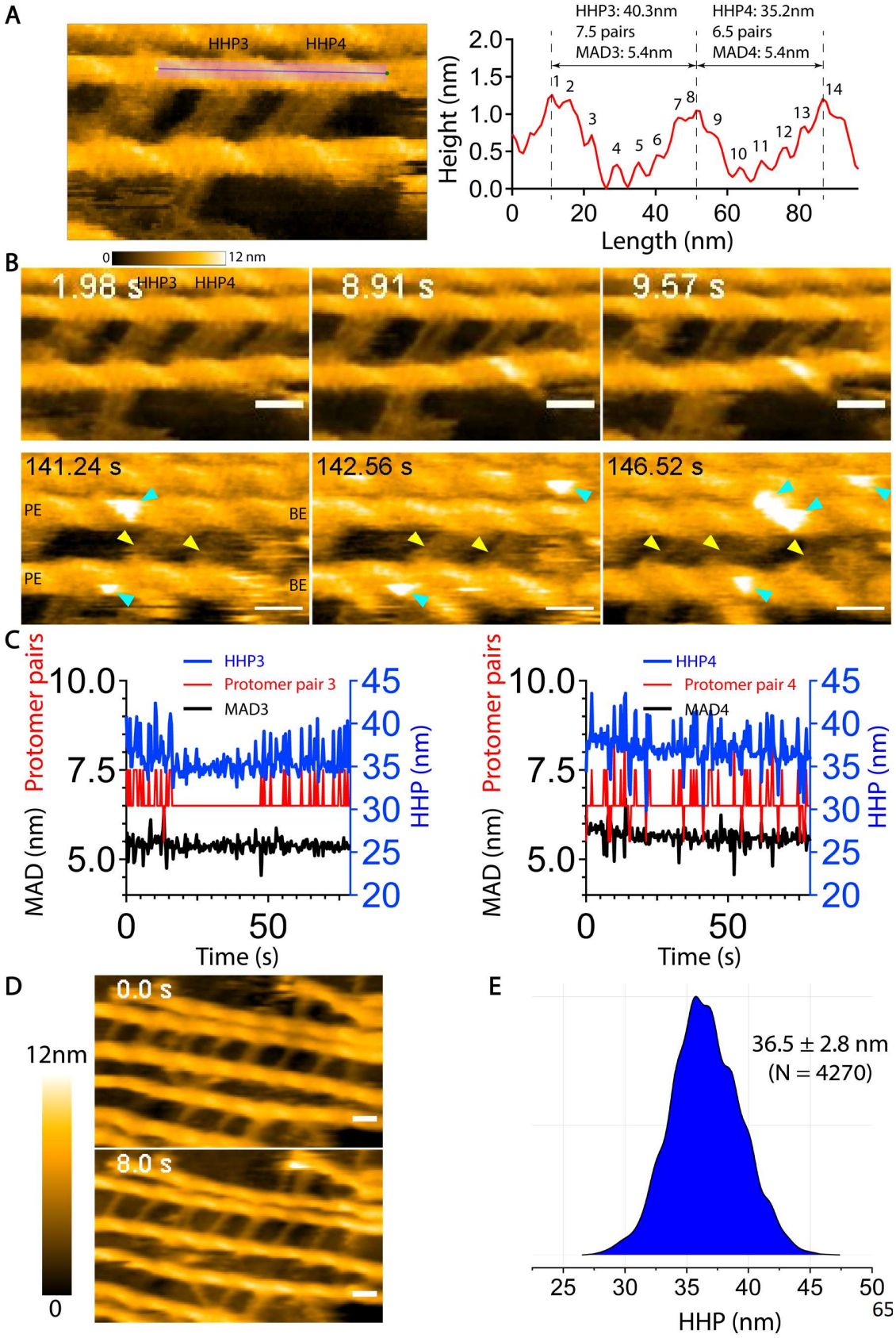
A
HHP3
HHP4
HHP3: 40.3nm
7.5 pairs
MAD3: 5.4nm
HHP4: 35.2nm
6.5 pairs
MAD4: 5.4nm
Height (nm)
Length (nm)
B
0
12 nm
1.98 s
HHP3
HHP4
8.91 s
9.57 s
141.24 s
142.56 s
146.52 s
PE
BE
C
Protomer pairs
HHP3
Protomer pair 3
MAD3
MAD (nm)
HHP (nm)
Time (s)
HHP4
Protomer pair 4
MAD4
D
12nm
0.0 s
8.0 s
E
36.5 ± 2.8 nm
(N = 4270)
HHP (nm)

1643 **Supplementary Figure 1: Analysis of the dynamic conformations of actin**
1644 **filaments crosslinked by alpha-actinin in unipolar configuration in the**
1645 **presence or absence of S1 using HS-AFM.**
1646 (**A**) A longitudinal section profile illustrating for the analysis of two consecutive
1647 HHPs, the number of protomer pairs per HHP, and MADs in various actin filaments
1648 captured at different time points. The analytic methods used were developed in
1649 our previous study[24].
1650 (**B**) Still AFM images with time labels were shown for conditions with ATP present
1651 and after ATP depletion (primarily converted into ADP and inorganic phosphate in
1652 solution) to observe the binding of S1 on actin filaments. As ATP levels gradually
1653 declined or nearly depleted due to ATP hydrolysis (ATP → ADP + Pi) during the
1654 actomyosin reaction, S1 binding to actin filaments persisted for longer durations,
1655 enabling capture by HS-AFM at an imaging rate of 330 ms per frame. All actin
1656 filaments in the imaging field were aligned with the pointed end (PE) on the left
1657 and the barbed end (BE) on the right, reflecting the actual unipolar crosslinking
1658 configuration. As similarly done in our previous study[22] by referring to the EM
1659 study[67], the polarity of actin filaments was confirmed by observing the tilted angles
1660 of S1, with its head pointing toward the pointed (minus) end (PE), resembling an
1661 arrowhead along the filament. This characteristic orientation allowed differentiation
1662 between the PE and the barbed (plus) end (BE). Yellow and cyan arrowheads
1663 indicate alpha-actinin and S1 molecules, respectively. Scale bars: 25 nm. Color
1664 scale: 0-12 nm.
1665 **(C)** Time-dependent changes in two consecutive HHPs, the number of protomer
1666 pairs per HHP, and MADs in actin filaments crosslinked by 50 nM α-actinin in the
1667 presence of 1 mM ATP, 0.1 mM $CaCl_2$, and 1 μM S1, but without $MgCl_2$.
1668 **Related to Fig. 2, Supplementary Video 2**.

(**D**) Still AFM images of actin filaments crosslinked using 50 nM alpha-actinin and imaged in F-buffer with 0.5 mM $MgCl_2$ and 0.5 mM ATP, but without $CaCl_2$. The polarity of the crosslinking configuration was determined based on a previous study [63]. Accordingly, the crosslinking of actin filaments by alpha-actinin was determined as unipolar configuration in this case. It is because no changes were observed in the preferred attachment angle of the crosslinkers once the filament spacing stabilized, indicating that the filaments were incorporated in the same polarity as previously crosslinked filaments (an unipolar configuration). Scale bars: 25 nm. Color scale: 0-12 nm. Related to **Supplementary Video 3**.

(**E**) A histogram of HHP measured for actin filaments crosslinked with alpha-actinin. A total of 4270 HHPs were counted.

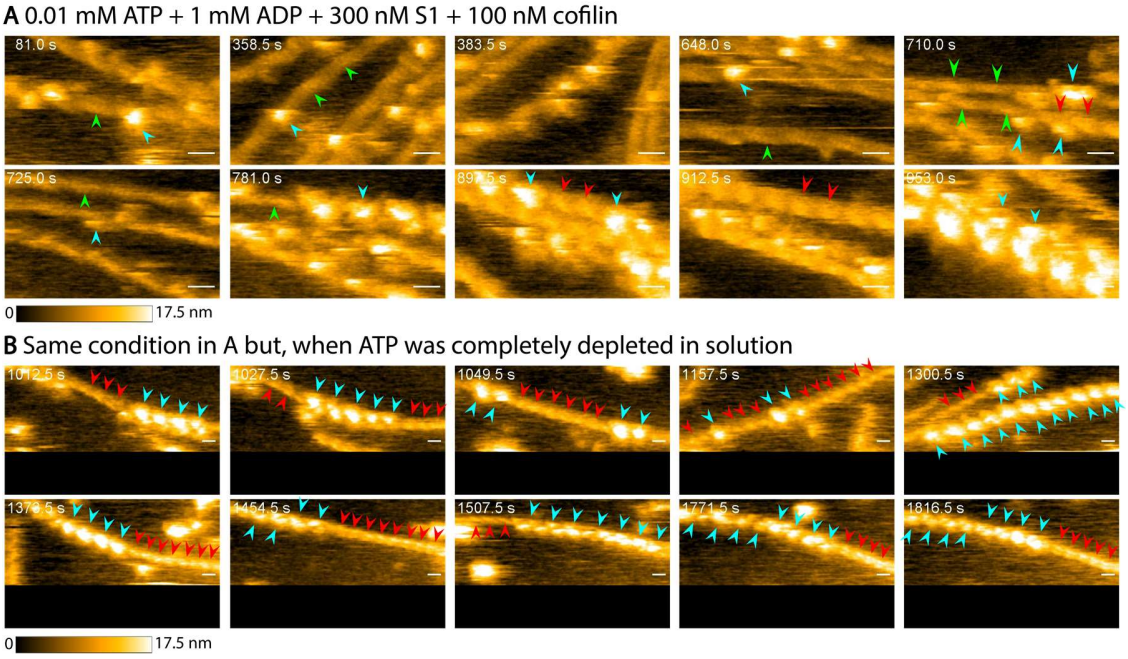

Supplementary Figure 2: Segregation of cofilin and S1 clusters, as identified by their distinct short and long HHP conformations and corresponding peak-height differences, visualized using HS-AFM.

(**A**) Cofilin and S1 competitively interact and utilize different HHP structures on the same actin filament to form their respective clusters. Green, cyan, and red arrowheads denote bare actin (lowest height, normal HHP), S1-actin (highest height, normal HHP), and cofilactin (intermediate height between bare actin and S1-actin, with a ~25% reduction in HHP) those are represented in these still AFM images. Actin filaments were initially imaged in F-buffer containing 0.01 mm ATP, 1 mM ADP, and 300 nM S1, followed by adding 100 nM cofilin. As ATP levels gradually declined due to ATP hydrolysis (ATP → ADP + Pi) during the actomyosin reaction, S1 binding to actin filaments persisted for longer durations and formed stable its clusters when ATP was completely depleted. Time indicates the time after adding cofilin before (**upper panel**) and after (**lower panel**) ATP was completely depleted in solution. Scale bars: 25 nm. Color scales: 0-17.5 nm. **Related to Fig. 3D-F, Supplementary Videos 5 and 6**.

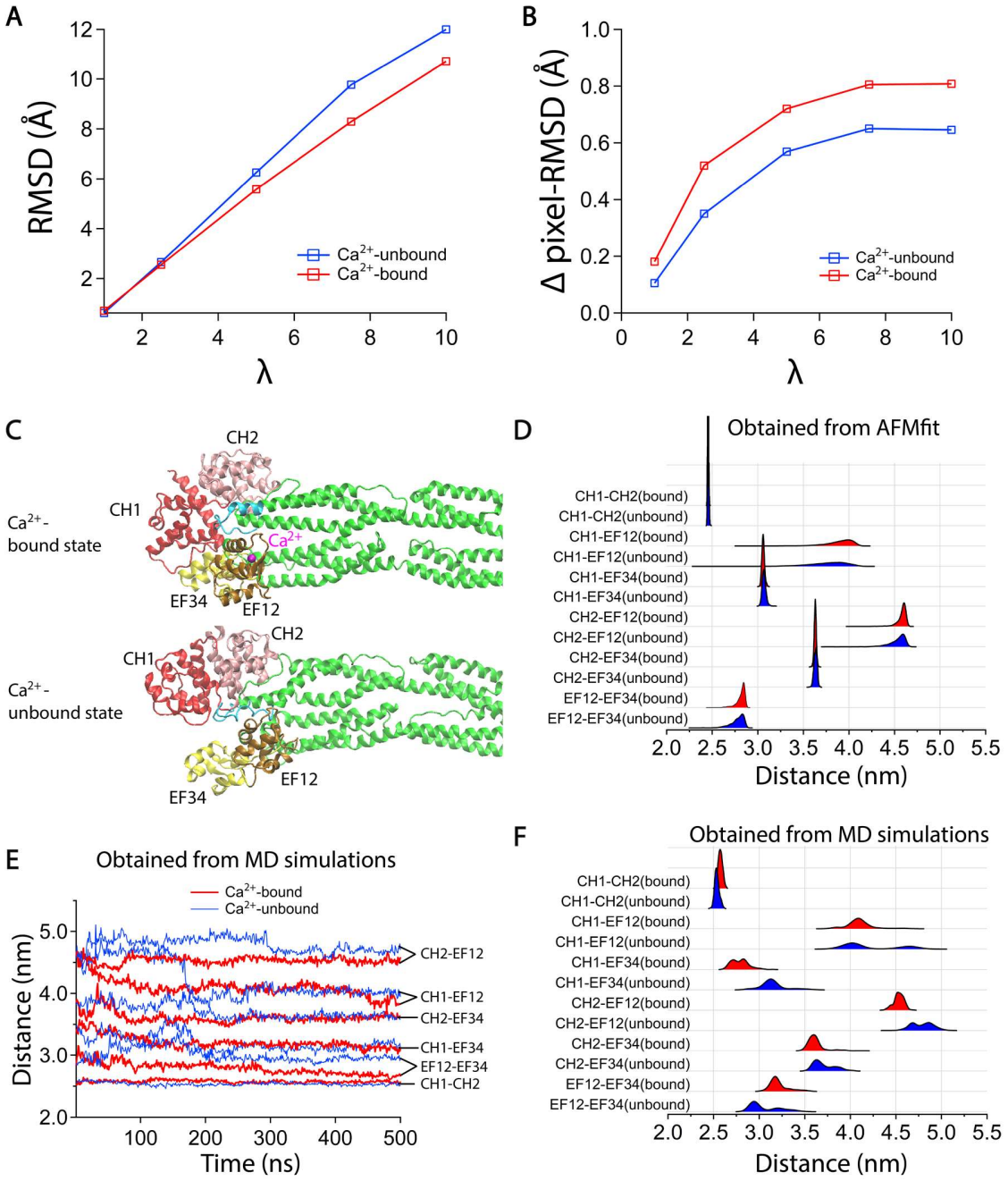

Supplementary Figure 3: Analysis of domain distances in Ca^{2+}-bound and Ca^{2+}-unbound alpha-actinin based on conformations obtained from AFMfit and MD simulations.

(**A**) Results of the exhaustive search for the optimal value of a hyperparameter (λ). Average root mean square deviation (RMSD): This represented the average amplitude of the flexible deformation, calculated as the RMSD between the final and initial states. The largest λ value tested that keeps the average RMSD below 10 Å is λ = 7.5.

(**B**) Average Pixel-RMSD Difference: This corresponded to the criterion used by AFMfit to evaluate the goodness of fit. Beyond λ = 7.5, the fitting ceases to improve and reaches a plateau, indicating the onset of overfitting (See Supplementary Methods). **Related to Supplementary Videos 7-8.**

(**C**) Structural comparison of Ca^{2+}-bound and Ca^{2+}-unbound alpha-actinin, showing the positions of the CH1, CH2, EF12, and EF34 domains.

(**D**) Distribution of distances between the CH1, CH2, EF12, and EF34 domains in Ca^{2+}-bound (N = 1466) and Ca^{2+}-unbound (N = 1140) alpha-actinin derived from AFMfit conformations. The domain distances were measured separately for chain 1 and chain 2 in individual conformations (stored as PDB files) for both Ca^{2+}-bound and Ca^{2+}-unbound states. The final data represent the averaged values of the two chains. Related to **Supplementary Table 1**.

(**E, F**) Time-dependent variations and distributions of domain distances between the CH1, CH2, EF12, and EF34 domains in Ca^{2+}-bound (N = 500) and Ca^{2+}-unbound (N = 500) alpha-actinin, based on conformations from MD simulations. The domain distances were similarly measured for chain 1 and chain 2 in individual conformations for both Ca^{2+}-bound and Ca^{2+}-unbound states. The final data represent the averaged values of the two chains. Related to **Supplementary Table 1**.

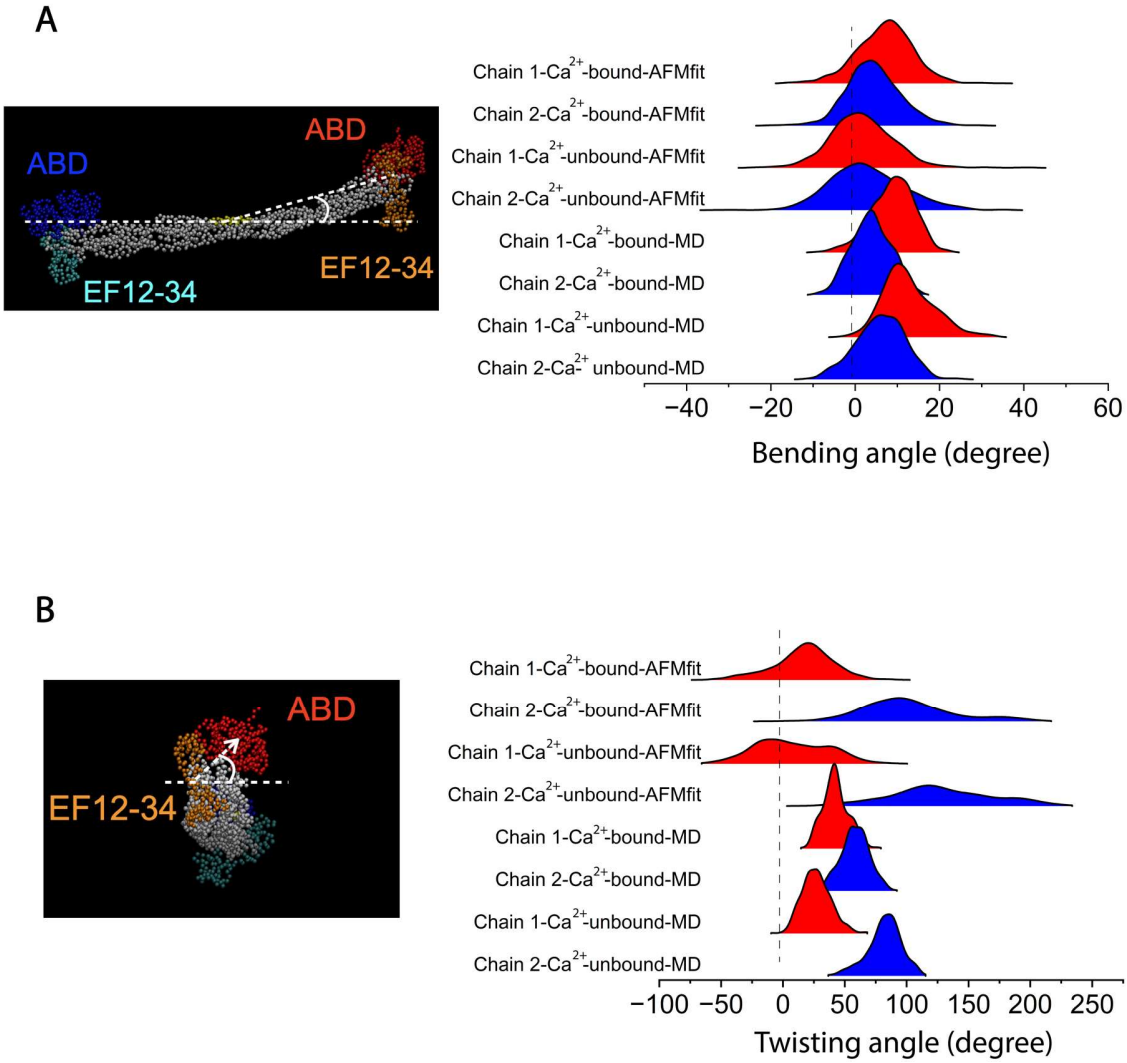

Supplementary Figure 4: Analysis of the bending and twisting angles of the ABD relative to the rod domain of Ca^{2+}-bound and Ca^{2+}-unbound alpha-actinin using the conformations obtained from (A) AFMfit and (B) MD simulations (MD).

PCA of the conformations confirmed the rigidity of the rod domain (SR2-SR3). To calculate the bending and twisting angles, a reference vector (dashed line) was aligned along the Cα positions within the SR2-SR3 domain, defining 0 degrees. The bending angles were then determined relative to the center of mass of the Cα atoms in the CH1, CH2, EF12, and EF34 domains near the neck domain in chain 1 (red) and chain 2 (blue), as shown in the upper panels (A). For the twisting angles, a vector was defined by connecting the centers of mass of the Cα atoms between the EF12-EF34 and CH1-CH2 domains. These twisting angles were then measured relative to a reference vector aligned along the SR2-SR3 domain, as shown in the upper panel (B). Positive and negative bending or twisting angles corresponded to angles in the upper and lower reference vectors, respectively, for both (A) and (B). A two-population *t-test* was conducted to evaluate the statistical difference ($p < 0.05$) between the mean values of the Ca^{2+}-bound and Ca^{2+}-unbound states. Related to **Supplementary Table 1**.

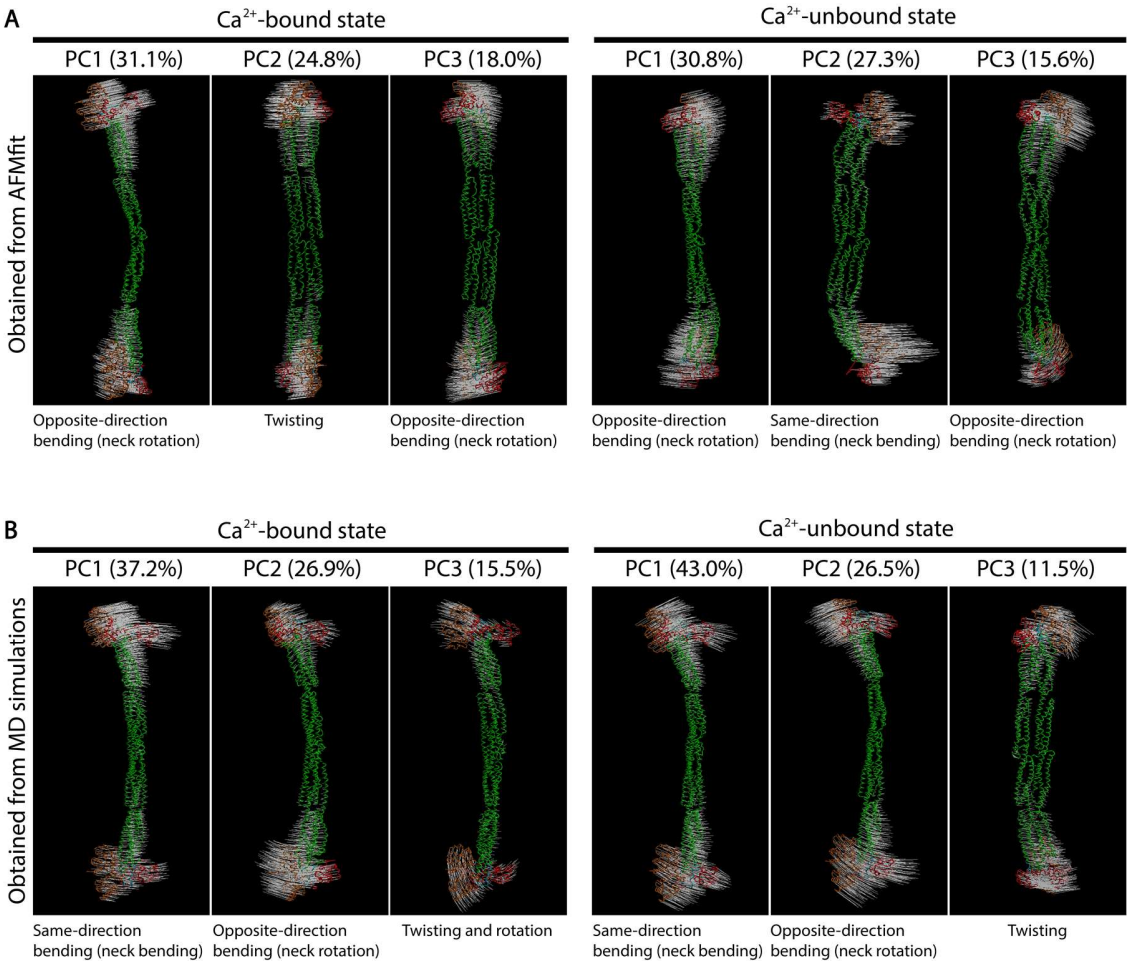

Supplementary Figure 5: PCA of atomic structures and physical motions of Ca^{2+}-bound and Ca^{2+}-unbound alpha-actinin using conformational libraries obtained from AFMfit and MD simulations. The PCA was conducted using conformations of Ca^{2+}-bound and Ca^{2+}-unbound states, obtained from AFMfit (A) and MD simulations (B).

Eigenvalues of the principal components (PC1, PC2, PC3) were used to calculate the contribution in percentage of each physical motion for these states. The alpha-actinin structures are illustrated in tube conformations, with the ABD, neck, rod, and EF12-EF34 domains represented in red, cyan, green, and yellow, respectively. Eigenvectors indicating the direction of motion are shown with white arrows. Related to **Supplementary Videos 12-15**.

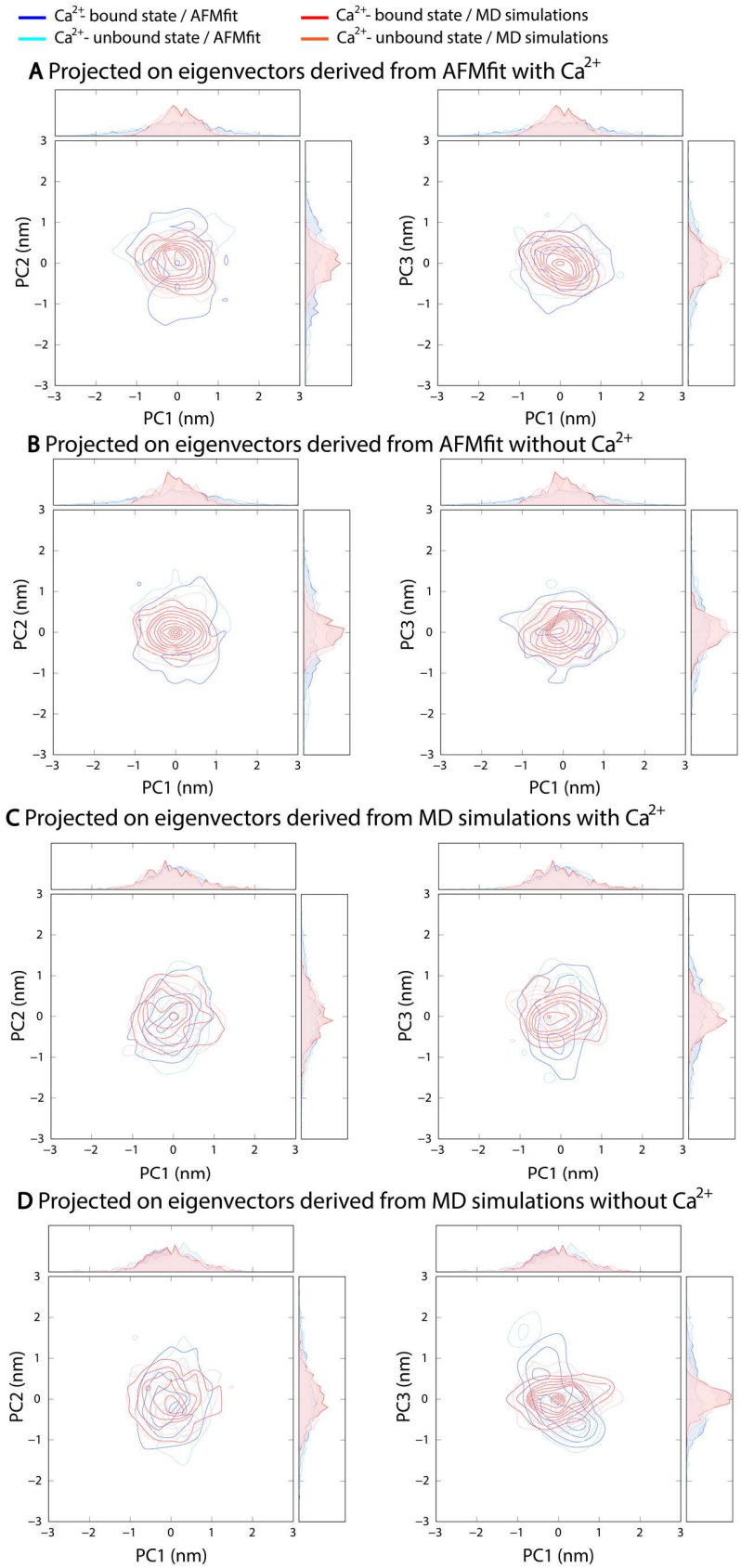
Ca2+- bound state / AFMfit
Ca2+- unbound state / AFMfit
Ca2+- bound state / MD simulations
Ca2+- unbound state / MD simulations
A Projected on eigenvectors derived from AFMfit with Ca2+
B Projected on eigenvectors derived from AFMfit without Ca2+
C Projected on eigenvectors derived from MD simulations with Ca2+
D Projected on eigenvectors derived from MD simulations without Ca2+
PC1 (nm)
PC2 (nm)
PC3 (nm)

1800

1801 **Supplementary Figure 6: The ensemble motions of atomic conformations**
1802 **and distributions of principal components of alpha-actinin with Ca^{2+}-bound**
1803 **and Ca^{2+}-unbound states obtained from AFMfit and MD simulations**
1804 **projected onto four PCA spaces.**
1805 All the libraries of conformations with and without Ca^{2+} obtained from AFMfit and
1806 MD simulations were projected onto eigenvectors derived from either the data with
1807 Ca^{2+} obtained from AFMfit (**A**), or from the data without Ca^{2+} obtained from AFMfit
1808 (**B**), or from the data with Ca^{2+} obtained from MD simulations (**C**), or from the data
1809 without Ca^{2+} obtained from MD simulations (**D**). The plots in dark blue, light blue,
1810 dark red, and light red are the projections of the conformations with Ca^{2+} obtained
1811 from AFMfit, without Ca^{2+} obtained from AFMfit, with Ca^{2+} obtained from MD
1812 simulations, and without Ca^{2+} obtained from MD simulations, respectively. Related
1813 to **Supplementary Fig. 5**.
1814
1815
1816
1817
1818
1819

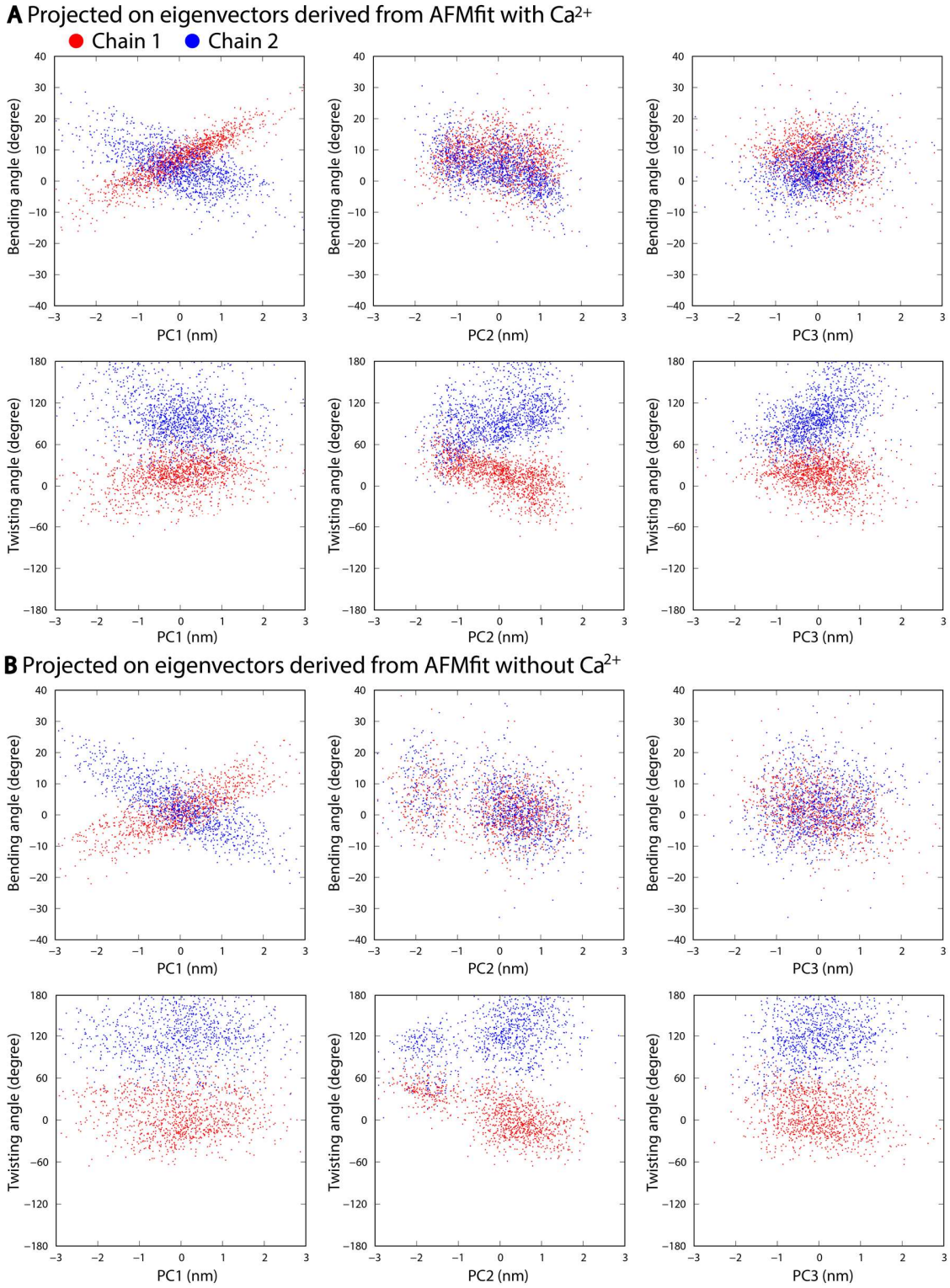
A Projected on eigenvectors derived from AFMfit with Ca2+
Chain 1
Chain 2
Bending angle (degree)
Twisting angle (degree)
PC1 (nm)
PC2 (nm)
PC3 (nm)
B Projected on eigenvectors derived from AFMfit without Ca2+

1820

1821 **Supplementary Figure 7: Correlation between principal components (PC1,**
1822 **PC2, PC3) and bending and twisting angles in Ca^{2+}-bound and Ca^{2+}-unbound**
1823 **alpha-actinin using conformations obtained from AFMfit.** Related to
1824 **Supplementary Fig. 4, 5**.
1825 (**A, B**) The plots of the correlation between PC1, PC2, PC2 and bending and
1826 twisting angles in chain 1 (red dots) and chain 2 (blue dots) of Ca^{2+}-bound and
1827 Ca^{2+}-unbound alpha-actinin obtained from AFMfit.
1828
1829
1830
1831
1832
1833
1834
1835
1836
1837
1838
1839
1840
1841
1842
1843
1844
1845
1846
1847
1848
1849
1850

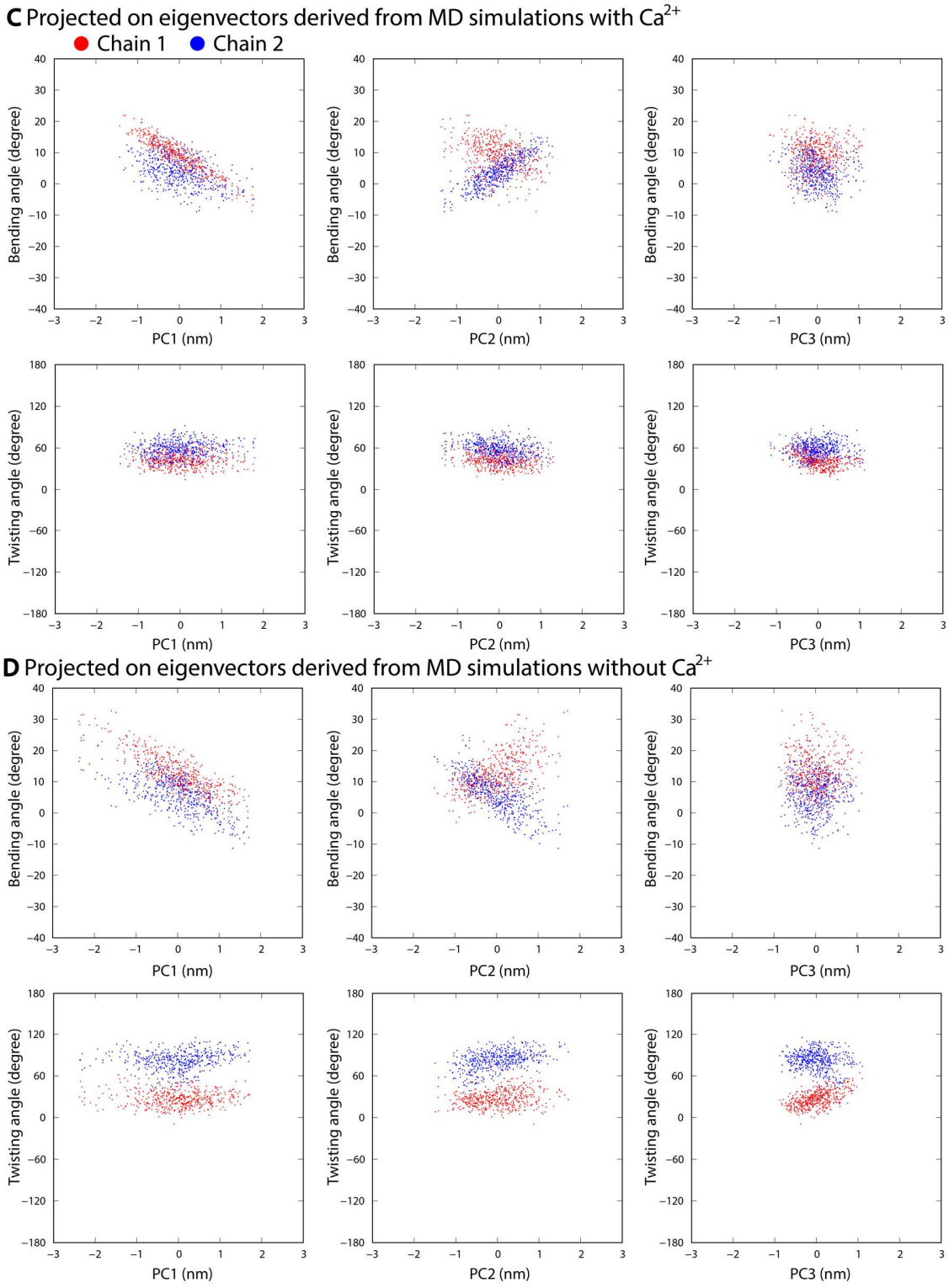
C Projected on eigenvectors derived from MD simulations with Ca2+
Chain 1
Chain 2
Bending angle (degree)
Twisting angle (degree)
PC1 (nm)
PC2 (nm)
PC3 (nm)
D Projected on eigenvectors derived from MD simulations without Ca2+

1851

1852 **Supplementary Figure 8: Correlation between principal components (PC1,**
1853 **PC2, PC3) and bending and twisting angles in Ca^{2+}-bound and unbound**
1854 **alpha-actinin using conformations obtained from MD simulations**. Related to
1855 **Supplementary Fig. 4, 5**.
1856 (**C, D**) The plots of the correlation between PC1, PC2, PC2 and bending and
1857 twisting angles in chain 1 (red dots) and chain 2 (blue dots) of Ca^{2+}-bound and
1858 Ca^{2+}-unbound alpha-actinin obtained from MD simulations.
1859
1860
1861
1862
1863
1864
1865
1866
1867
1868
1869
1870
1871
1872
1873
1874
1875
1876
1877
1878
1879
1880
1881

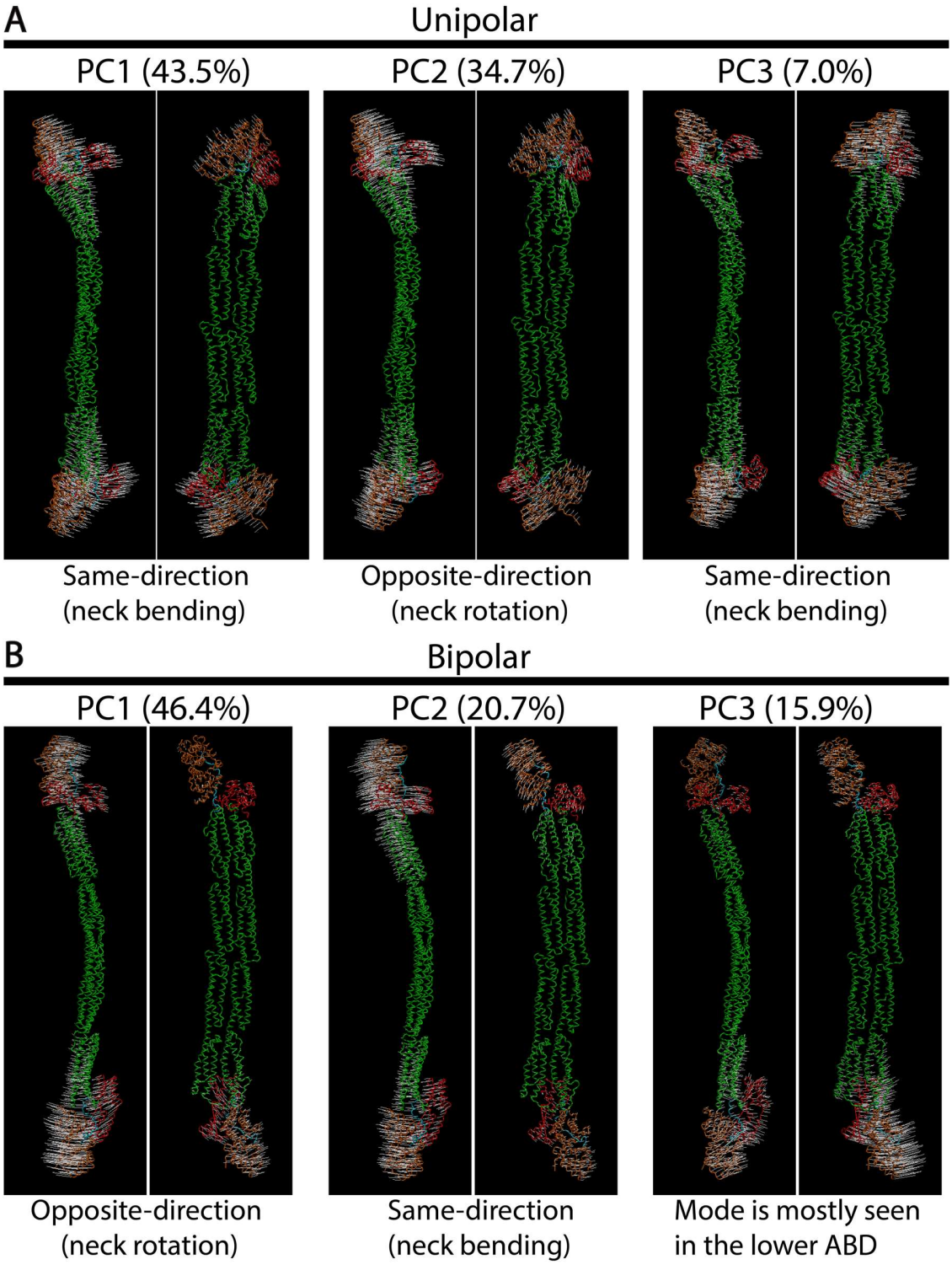
A
Unipolar
PC1 (43.5%)
PC2 (34.7%)
PC3 (7.0%)
Same-direction
(neck bending)
Opposite-direction
(neck rotation)
Same-direction
(neck bending)
B
Bipolar
PC1 (46.4%)
PC2 (20.7%)
PC3 (15.9%)
Opposite-direction
(neck rotation)
Same-direction
(neck bending)
Mode is mostly seen
in the lower ABD

1882

1883 **Supplementary Figure 9: PCA of the atomic structures and physical motions**
1884 **of alpha-actinin molecules on the basis of conformational libraries derived**
1885 **from unipolar (A) and bipolar (B) crosslinking models obtained with MD**
1886 **simulations.**
1887 The alpha-actinin structures are illustrated in tube conformations, with the ABD,
1888 neck, rod, and EF12-EF34 domains represented in red, cyan, green, and yellow,
1889 respectively. Eigenvectors indicating the direction of motion are shown with white
1890 arrows. The final system of unipolar configurations consisted of two actin fibers (26
1891 protomers), one alpha-actinin molecule, 1032 K^+ atoms, 718 Cl^- atoms, 26 Mg^{2+}
1892 atoms, 26 ADP molecules, and 1,433,011 water molecules, for a total number of
1893 4,479,739 atoms in the system. The bipolar model was constructed similarly,
1894 differing only in the inclusion of 1,432,853 water molecules (see Supplementary
1895 Methods). Related to **Supplementary Videos 16-17**.
1896
1897
1898
1899
1900
1901
1902
1903
1904
1905
1906
1907
1908
1909
1910
1911
1912

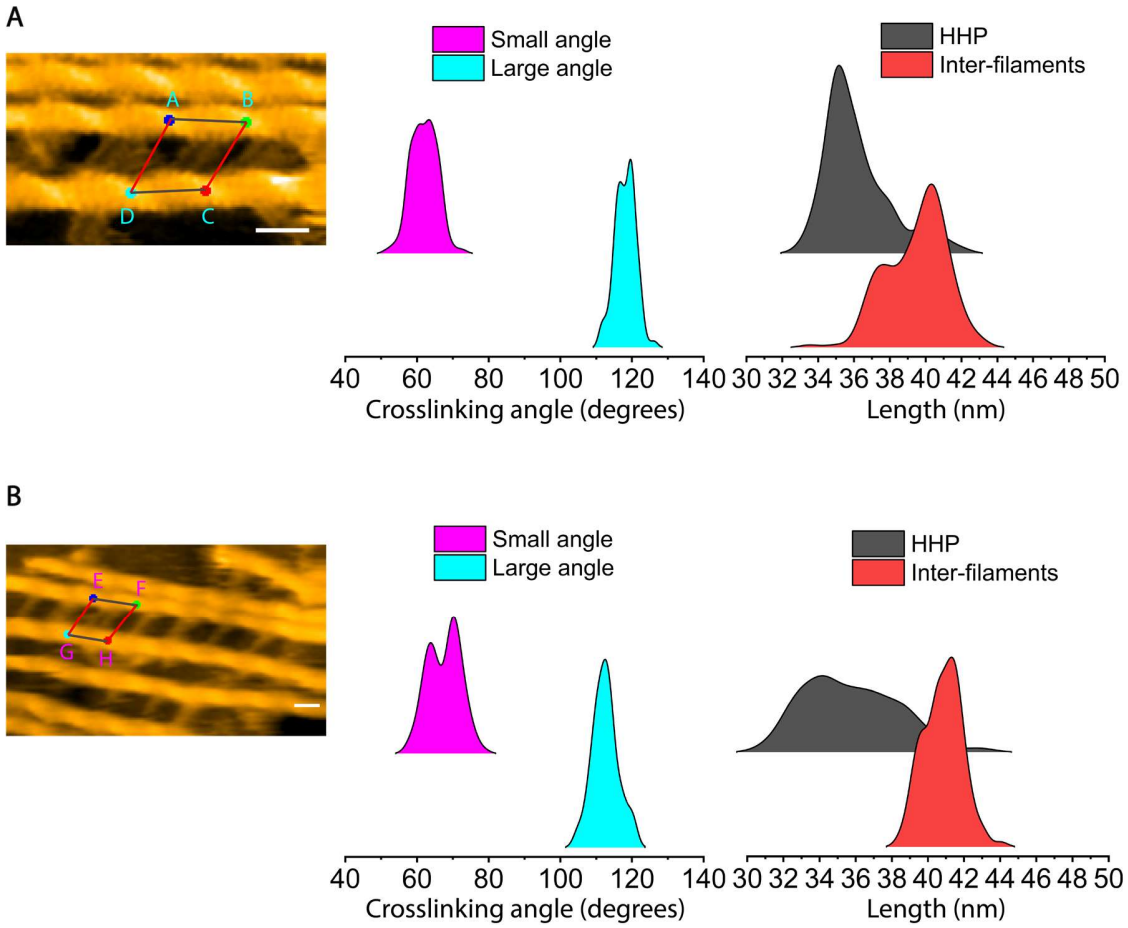

Supplementary Figure 10: Quantitative analysis of spacious inter-filament lengths, HHP, and alpha-actinin crosslinking angles relative to the filament axis, based on experimental HS-AFM data for actin filaments crosslinked by alpha-actinin, both in the presence (A) and absence (B) of S1.

1918 In our HS-AFM data, alpha-actinin crosslinked the actin filaments in a unipolar
1919 configuration. Two alpha-actinin molecules consistently intercalated between actin
1920 filaments at every half-helical turn, forming a parallelogram-like configuration. The
1921 segments AB, CD, EF, and HG correspond to HHP, while AD, BC, EG, and FH
1922 represent inter-filament spaces or lengths. It is noted that the definition of inter-
1923 filament spacing differs slightly from that in the MD simulation data (**Fig. 5B**). In
1924 the MD simulation, spacing was measured by a vertical line connecting between
1925 the two filaments, whereas in the AFM data, it is determined by measuring the
1926 parallel sides of a parallelogram. As a result, the inter-filament lengths measured
1927 in AFM data were larger than that in MD simulations. Statistical differences were
1928 assessed using a two-population t-test, with a significant difference confirmed at p
1929 ≤ 0.05. See our analysis in Supplementary Methods for details. Related to **Fig. 2,**
1930 **Supplementary Fig. 1, Supplementary Table 1, and Supplementary Videos 2–**
1931 **3**.
1932 **Supplementary Table 2** A brief comparison of structure, localization, and
1933 functions of actin filaments crosslinked by alpha-actinin in bipolar and unipolar
1934 configurations within cells[61–63,67,108]. Related to **Figure 6B**.

Feature	Bipolar configuration	Unipolar configuration
Polarity	Opposite at each end	All barbed (plus) ends face the same direction
Crosslinking by alpha-actinin	Forms contractile networks	Forms stable, non-contractile bundles
Myosin interaction	Strong (contractile activity)	Weak (non-contractile activity)
Cellular function	Force generation, contraction	Protrusion, structural support, migration
Localization in cells	Stress fibers, contractile rings, sarcomeres	Lamellipodia, filopodia, cortical actin, microvilli

1937 **Supplementary Video 1** HS-AFM imaging of structure and dynamic
1938 conformational changes of Ca^{2+}-bound and Ca^{2+}-unbound alpha-actinin in
1939 solution. The AFM images were smoothed with Gaussian filter (σ = 1). Imaging
1940 rate was done at 100 ms per frame. The Supplementary Video plays at 5 fps. Scale
1941 bars: 25 nm. Related to **Fig. 2**.
1942 **Supplementary Video 2** HS-AFM imaging of the dynamic conformational
1943 changes in actin filaments crosslinked by alpha-actinin in the presence of ATP,
1944 Ca^{2+}, and S1. Actin filaments were incubated with 50 nM α-actinin under conditions
1945 containing 1 mM ATP, 0.1 mM $CaCl_2$, and 1 μM S1, but without $MgCl_2$. As ATP
1946 levels gradually declined or nearly depleted due to ATP hydrolysis (ATP → ADP +
1947 Pi) during the actomyosin reaction, S1 binding to actin filaments persisted for
1948 longer durations, enabling capture by HS-AFM at an imaging rate of 330 ms per
1949 frame. All actin filaments in the imaging field were aligned with the pointed end
1950 (PE) on the left and the barbed end (BE) on the right, reflecting the actual unipolar
1951 crosslinking configuration. The polarity of actin filaments was determined using S1,
1952 as similarly done in our previous study[22] by referring to the EM study[67]. The AFM
1953 images were processed using a Gaussian filter (σ = 1). The Supplementary Video
1954 plays at 5 frames per second. Scale bar: 25 nm. Related to **Fig. 2, Supplementary**
1955 **Fig. 1A-C**.
1956 **Supplementary Video 3** HS-AFM imaging of the dynamic conformational
1957 changes in actin filaments crosslinked by alpha-actinin in the presence of ATP and
1958 Mg^{2+}. Actin filaments were crosslinked with 50 nM alpha-actinin and observed in
1959 F-buffer supplemented with 0.5 mM $MgCl_2$ and 0.5 mM ATP, but without $CaCl_2$.
1960 The AFM images were recorded at an imaging rate of 500 ms per frame and
1961 processed using a Gaussian filter (σ = 1). The Supplementary Video plays at 5
1962 frames per second. Scale bar: 25 nm. Related to **Supplementary Fig. 1D-E**.

1963 **Supplementary Video 4** HS-AFM analysis of helical structures in actin filaments
1964 without and with alpha-actinin crosslinking. Actin filaments were gently
1965 immobilized on a lipid membrane and imaged in F-buffer containing 1 mM ATP,
1966 600 nM hs cofilin, and either (A) without or (B) with 400 nM alpha-actinin. Alpha-
1967 actinin crosslinking was found to suppress the shortening of half helices and the
1968 formation of mature cofilin clusters. AFM images were captured at an imaging rate
1969 of 500 ms per frame and processed with a Gaussian filter (σ = 1). Time labels
1970 indicate the elapsed time after cofilin addition. The Supplementary Video plays at
1971 5 frames per second. Scale bar: 25 nm. Related to **Fig. 3A-C**.
1972 **Supplementary Video 5** HS-AFM imaging was conducted to explore the
1973 competitive interactions between cofilin and S1, focusing on how they utilize
1974 distinct helical structures on the same actin filament to form their respective
1975 clusters. Actin filaments were gently immobilized on a lipid membrane and imaged
1976 in F-buffer initially containing 1 mM ADP, 0.01 mM ATP, and 300 nM S1, followed
1977 by the addition of 100 nM cofilin. When ATP was gradually or nearly depleted,
1978 stable S1 clusters were formed near cofilin clusters on actin filaments. AFM images
1979 were acquired at a rate of 500 ms per frame and processed using a Gaussian filter
1980 (σ = 1). Time labels indicate the elapsed time after cofilin addition. The
1981 Supplementary Video plays at 5 frames per second, with a scale bar of 25 nm.
1982 Related to **Fig. 3D, Supplementary Fig. 2**.
1983 **Supplementary Video 6** HS-AFM imaging was performed to observe actin
1984 filaments utilizing distinct shorter and longer half-helices for the binding of cofilin
1985 clusters and S1 clusters, respectively. Actin filaments were gently immobilized on
1986 a lipid membrane and imaged in F-buffer initially containing 1 mM ADP, 0.01 mM
1987 ATP, and 300 nM S1, followed by the addition of 100 nM cofilin. As ATP levels
1988 completely depleted, stable S1 clusters formed in proximity to cofilin clusters on
1989 the same actin filaments. AFM images were recorded at a rate of 500 ms per frame
1990 and processed using a Gaussian filter (σ = 1). Time labels indicate the elapsed
1991 time after cofilin addition. The Supplementary Video plays at 5 frames per second.
1992 Scale bar: 25 nm. Related to **Fig. 3D**.

1993 **Supplementary Video 7** The HS-AFM Supplementary Videos of Ca^{2+}-bound
1994 alpha-actinin (left) and the atomic model (right) that were obtained through rigid
1995 and flexible fitting using AFMfit. The initial model of the Ca^{2+}-bound state was
1996 constructed based on PDB entry 1SJJ. Related to **Fig. 4A**.
1997 **Supplementary Video 8** The HS-AFM Supplementary Videos of Ca^{2+}-unbound
1998 alpha-actinin (left) and the atomic model (right) that were obtained through rigid
1999 and flexible fitting using AFMfit. The initial model of the Ca^{2+}-unbound state was
2000 generated based on PDB entry 1SJJ. Related to **Fig. 4A**.
2001 **Supplementary Video 9** PC1 captured the ensemble of opposite-direction
2002 bending motions or neck rotation. Related to **Fig. 4C**.
2003 **Supplementary Video 10** PC2 represented same-direction bending motions or
2004 neck bending. Related to **Fig. 4C**.
2005 **Supplementary Video 11** PC3 described a combination of opposite-direction
2006 bending and twisting motions. Related to **Fig. 4C**.
2007 **Supplementary Video 12** PC1, PC2, PC3 described physical motions Ca^{2+}-bound
2008 alpha-actinin obtained from AFMfit. Related to **Supplementary Fig. 5A**.
2009 **Supplementary Video 13** PC1, PC2, PC3 described physical motions Ca^{2+}-
2010 unbound alpha-actinin obtained from AFMfit. Related to **Supplementary Fig. 5A**.
2011 **Supplementary Video 14** PC1, PC2, PC3 described physical motions Ca^{2+}-bound
2012 alpha-actinin obtained from MD simulations. Related to **Supplementary Fig. 5B**.
2013 **Supplementary Video 15** PC1, PC2, PC3 described physical motions Ca^{2+}-
2014 unbound alpha-actinin obtained from MD simulations. Related to **Supplementary**
2015 **Fig. 5B**.
2016 **Supplementary Video 16** PC1, PC2, PC3 described physical motions Ca^{2+}-
2017 unbound alpha-actinin, as derived from unipolar crosslinking model obtained from
2018 MD simulations. Related to **Supplementary Fig. 9A**.
2019 **Supplementary Video 17** PC1, PC2, PC3 described physical motions Ca^{2+}-
2020 unbound alpha-actinin, as derived from bipolar crosslinking model obtained from
2021 MD simulations. Related to **Supplementary Fig. 9B**.

2022 **Supplementary Video 18** Molecular dynamics of unipolar-flexible crosslinking
2023 model obtained from MD simulations. All atoms were allowed to flexibly vibrate in
2024 the model and MD simulations were carried out for 100 ns. With different residue
2025 contacts locating in different domains on both sides of actin subunits (e.g.,
2026 electrostatic interaction between actin: ASP25, ARG28, GLU57, ARG95, GLU99,
2027 GLN354 and alpha-actinin: ARG233, GLU236, LYS122, ASP27/GLU236, LYS107,
2028 ARG87) compared to the bipolar-flexible model, alpha-actinin-unbound Ca^{2+}
2029 appeared to promote greater same-direction neck bending (PC1 + PC3: 50.5%)
2030 than opposite-direction neck rotation (PC2: 34%) in the unipolar-flexible model.
2031 This suggests that alpha-actinin's bending or rotation may have minimal impact on
2032 fluctuations in rise and AD in the unipolar model compared to the two bipolar
2033 models, which displayed specific electrostatic interactions between residues (e.g.,
2034 actin: ARG28, GLU57, ARG95; alpha-actinin: GLU149, ARG233,
2035 GLU31/GLU149/ASP235). Moreover, the rise fluctuations were nearly identical to
2036 those observed in the bare actin filament, but AD fluctuations were significantly
2037 different ($p \leq 0.05$). **Note**: The simulation box remained unchanged. Consequently,
2038 slight drifting of the model in the box may cause the actin protomers to move in or
2039 out of the box. Related to **Fig. 5, Supplementary Fig. 9, Supplementary Table**
2040 **1**.

2041 **Supplementary Video 19** Molecular dynamics of bipolar-flexible crosslinking
2042 model obtained from MD simulations. All atoms were allowed to flexibly vibrate in
2043 the model and MD simulations were carried out for 100 ns. With specific residue
2044 contacts locating in different domains on both sides of actin subunits and different
2045 locations compared to the unipolar-flexible model, alpha-actinin-unbound Ca^{2+}
2046 appeared to induce greater opposite-direction neck rotation (PC1: 46.4%) than
2047 same-direction neck bending (PC2: 20.7%) in the bipolar-flexible model. This
2048 suggests that neck rotation in alpha-actinin has a stronger physical impact on
2049 fluctuations in rise and AD, whereas the unipolar-flexible model exhibited weaker
2050 fluctuations in this motion. It is possible that certain key contacting residues
2051 contribute to this effect, warranting further investigation in future studies.
2052 Additionally, the rise and AD fluctuations were higher than those observed in the
2053 bare actin filament. **Note**: The simulation box remained unchanged. Consequently,
2054 slight drifting of the model in the box may cause the actin protomers to move in or
2055 out of the box. Related to **Fig. 5, Supplementary Fig. 9, Supplementary Table**
2056 **1**.
2057 **Supplementary Video 20** Molecular dynamics of bipolar-fixed crosslinking model
2058 obtained from MD simulations. In the model, all Cα atoms in alpha-actinin were
2059 computationally constrained to prevent vibrations, and MD simulations were
2060 performed for 100 ns. With less residue contacts and mainly electrostatic
2061 interactions between residues locating in different domains on both sides of actin
2062 subunits compared to the unipolar-flexible model, alpha-actinin-unbound Ca^{2+}
2063 exhibited highly rigid in the bipolar-fixed model. This explains that static
2064 electrostatic binding alpha-actinin to actin subunits in the bipolar model was
2065 sufficient to increase fluctuations in the rise and AD as compared to the flexible
2066 models. **Note**: The simulation box remained unchanged. Consequently, slight
2067 drifting of the model in the box may cause the actin protomer to move in or out of
2068 the box. Related to **Fig. 5, Supplementary Fig. 9, Supplementary Table 1**.
2069

2070 **Supplementary References**

2071 1. Ngo, K. X. *et al.* Deciphering the actin structure dependent preferential
2072 cooperative binding of cofilin. *Elife* **13**, 1–37 (2024).

2073 2. Ngo, K. X., Kodera, N., Katayama, E., Ando, T. & Uyeda, T. Q. Cofilin-
2074 induced unidirectional cooperative conformational changes in actin
2075 filaments revealed by high-speed atomic force microscopy. *Elife* **4**, 1–22
2076 (2015).

2077 3. David A. Begg, Richard Rodewald, L. I. R. The VISUALIZATION OF
2078 ACTIN FILAMENT POLARITY IN THIN SECTIONS Evidence for the
2079 Uniform Polarity of Membrane-Associated Filaments. *J. Cell Biol.* **79**, 846–
2080 852 (1978).

2081 4. Taylor, K. A., Taylor, D. W. & Schachat, F. Isoforms of α-actinin from
2082 cardiac, smooth, and skeletal muscle form polar arrays of actin filaments.
2083 *J. Cell Biol.* **149**, 635–645 (2000).

2084 5. Hampton, C. M., Taylor, D. W. & Taylor, K. A. Novel structures for α-
2085 actinin: F-actin interactions and their implications for actin-membrane
2086 attachment and tension sensing in the cytoskeleton. *J. Mol. Biol.* **368**, 92–
2087 104 (2007).

2088 6. Tojkander, S., Gateva, G. & Lappalainen, P. Actin stress fibers - Assembly,
2089 dynamics and biological roles. *J. Cell Sci.* **125**, 1855–1864 (2012).

2090 7. Rajan, S., Kudryashov, D. S. & Reisler, E. Actin Bundles Dynamics and
2091 Architecture. *Biomolecules* **13**, (2023).

2092